Cement and Concrete Research 203 (2026) 108160

Contents lists available at ScienceDirect

Cement and Concrete Research

journal homepage: www.elsevier.com/locate/cemconres

Effect of phase composition on the reactivity of DRI-EAF slags as SCM

Morteza Tayebi [a,*], Katrin Schollbach [a], J.C.O. Zepper [b], Stefan Melzer [c], H.J.H. Brouwers [a]

[a] Department of the Built Environment, Eindhoven University of Technology, P. O. Box 513, Eindhoven, 5600MB, the Netherlands
[b] Technical, Centre of Expertise, Steelmaking and Casting, Tata Steel Netherlands, PO Box 10000, IJmuiden, 1970CA, the Netherlands
[c] Tata Steel, P.O. Box 10000, IJmuiden, 1970CA, the Netherlands

ARTICLE INFO

Keywords:
Supplementary cementitious material (SCM)
Electric arc furnace (EAF) slag
Phase assemblage
Reactivity
Sustainable construction materials

ABSTRACT

DRI in EAFs will reduce the availability of blast-furnace slag, necessitating alternative SCMs. Five DRI–EAF slags (four engineered, and one industrial) were investigated, spanning $CaO/SiO_2 \approx 1.3$ or 2.0, FeOx ≈25 or 40 wt%, and cooling (air-cooled vs water-granulated). At 25 wt% clinker replacement, hydration and performance were quantified by isothermal and R^3 calorimetry, UPV, autogenous shrinkage, XRD/TGA, compressive strength, and leaching. Cooling history, through the control of the amorphous fraction, governed reactivity: water-granulated slags exhibited higher cumulative heat, accelerated set, and superior strength activity indices compared to air-cooled analogues. Basicity and FeOx exerted secondary effects: higher basicity accelerated hydration and reduced autogenous shrinkage, whereas elevated FeOx retarded reaction. All binders formed C–S–H, ettringite, and portlandite; hydrotalcite-like LDHs were detected only for the low-basicity, water-granulated slag. All mortars complied with Dutch leaching limits and met SCM strength benchmarks, evidencing the viability of engineered DRI–EAF slags as low-CO_2 cementitious binders.

1. Introduction

Cement and steel production, core pillars of modern infrastructure, are among the most carbon-intensive industrial processes worldwide [1–3]. Cement manufacturing alone contributes approximately 8% of global anthropogenic CO_2 emissions [4], primarily due to limestone calcination and the high thermal energy required for clinker production, derived mainly from fossil fuel combustion [5]. The steel industry adds a further 4–5% of emissions [4], primarily driven by the reliance on carbon-based reductants in ironmaking [6]. With global steel demand projected to rise from 1.9 Gt in 2020 to 2.4 Gt by 2100 [7], the urgency of decarbonizing these sectors is apparent.

A key transition in steelmaking is the shift from blast furnaces (BF) to electric arc furnaces (EAF) operating with direct reduced iron (DRI), increasingly using natural gas or hydrogen as the reductant [8]. While this transition lowers emissions, it will also reduce the availability of blast furnace slag, the source of ground granulated blast-furnace slag (GGBS), a widely used supplementary cementitious material (SCM) [9]. As EAFs and DRI replace blast furnaces, GGBS supply is expected to dwindle, creating an urgent need for alternative SCMs to maintain sustainable, low-CO_2 cement production [10]. Ore-based EAF slags, particularly from DRI-EAF processes, are a promising candidate. However, their application has been limited due to unclear chemical and phase characteristics compared with BF slag [11,12].

Conventional carbon-steel EAF slags are typically crystalline and dominated by CaO, FeO, SiO_2, and MgO [13] with limited reactivity. The mineralogy of EAF slags is variable, but commonly includes crystalline phases such as RO-Phase, magnetite, and Ca—Fe silicates, all of which react slowly under alkaline conditions [14]. Additionally, any Fe-bearing glass present dissolves poorly, further limiting reactivity. They also contain minor but environmentally relevant amounts of heavy metals such as chromium and vanadium, which can leach under alkaline conditions and thereby restrict their direct application in cementitious systems [15,16]. As a result, only a small fraction of steel slags (≈1%) is used in cementitious applications, compared with ≈70% for GGBS [14]. Early studies confirmed that replacing more than 15 wt% of cement with conventionally cooled EAF slag tends to lower early strength [17]. Even when finely ground, as granulated EAF slag often exhibits a significantly slower hydration rate and lower heat release than GGBS, particularly at early ages. These limitations have, until recently, limited most EAF slag to low-value uses, such as aggregates or fill, rather than as a cement substitute [18].

Recent advances in slag engineering suggest that reactivity can be enhanced by tailoring both chemistry and cooling history [19,20].

* Corresponding author.
E-mail address: m.tayebi@tue.nl (M. Tayebi).

https://doi.org/10.1016/j.cemconres.2026.108160
Received 14 October 2025; Received in revised form 2 February 2026; Accepted 3 February 2026
Available online 11 February 2026

Higher basicity (expressed as $B_2 = CaO/SiO_2$), typically favors the formation of Ca—Si phases such as larnite and bredigite, which can enhance reactivity. In contrast, excess Fe oxides tend to suppress hydration and stabilize inert spinels or RO-phase solid solutions [21]. Conventional air-cooling of EAF slag yields mostly crystalline melilite, merwinite, the RO phase, and β-C_2S, which react slowly [22,23]. Engineered slags with optimized chemistry and fast quenching have achieved amorphous contents above 80% and reactivities approaching those of GGBS [9,21]. Nevertheless, challenges remain. Fe-rich glass phases often dissolve slowly, MgO–FeO solid solutions can remain inert, and high B_2 must be moderated by Al_2O_3 or SiO_2 [21,24]. Processing innovations, such as hot-stage slag conditioning, flux modification, and combined quenching strategies, are being explored to mitigate these issues [12,24]. Several pilot-scale studies have already demonstrated that carefully engineered EAF slags can be transformed into SCMs with comparable strength development to blast-furnace slag [21,25–27]. However, these studies typically vary only a single parameter (e.g., chemistry or cooling) and rarely investigate their combined influence on hydration and performance. Furthermore, little is known about slags derived from emerging ore-based DRI-EAF processes, which are expected to differ from conventional scrap-based EAF slags in both composition and phase assemblage [13,25,28]. The coupled influence of Fe phases, B_2, and glass content on hydration kinetics, setting behavior, and mechanical properties, therefore, remains an open question.

The present study addresses this knowledge gap by investigating five representative slags: four engineered compositions systematically varied in B_2 ($CaO/SiO_2 \approx 1.3$ vs 2.0), Fe content (≈25 vs 40 wt% FeO_x), and cooling regime (air-cooled vs water-granulated), along with one industrial slag as a reference. Their hydration kinetics, phase evolution, setting times, autogenous shrinkage, strength development, and leaching behavior were systematically assessed. By linking calorimetry, microstructural analysis, and mechanical performance, this work provides an integrated view of how chemistry and processing jointly control reactivity. The findings not only clarify the relative roles of B_2, Fe content, and cooling but also offer guidance for designing next-generation EAF slags as reliable SCMs. Unlike prior studies that investigated isolated variables, this work employs a set of realistic DRI–EAF slag compositions and cooling regimes to provide a multivariate perspective on their reactivity as SCM.

2. Materials

2.1. Raw materials

Five EAF slags were investigated in this study, comprising four laboratory-engineered compositions produced by modifying an industrial slag precursor at the German Federal Institute for Materials Research and Testing (BAM, Berlin) and the slag used as a precursor as an industrial reference. The synthesis procedure was comparable to the method used in [29]. The water granulation of the slags was performed at the tapping of the pilot-scale EAF using a device developed at FEhS (Institut für Baustoff-Forschung), comparable to the one shown in [30]. The engineered EAF slag was tapped from the furnace into a runner. At the end of the runner, either a cast-iron mold was used (for air-cooled slags) or a water-bath box (for water-granulated slags). A specialized granulation rig was used to apply a water jet, generated through multiple outlet nozzles at the lower edge of a metallic ring. This ring was mounted on metallic pipes, one end closed and the other connected to a water supply, enabling operators to aim the water jet at the slag stream as it exited the runner. The jet intersected the molten slag stream just before it entered the water bath, promoting rapid cooling and glass formation. The visual appearance of the slags is shown in Fig. 1. Slags were formulated by varying the B_2 targeting two levels: low (~1.3) and high (~2.0), in combination with two levels of total iron oxide content (FeO_x): approximately 25 wt% (low Fe) and 40 wt% (high Fe), reflecting the compositional ranges in EAF steelmaking [13]. The selected

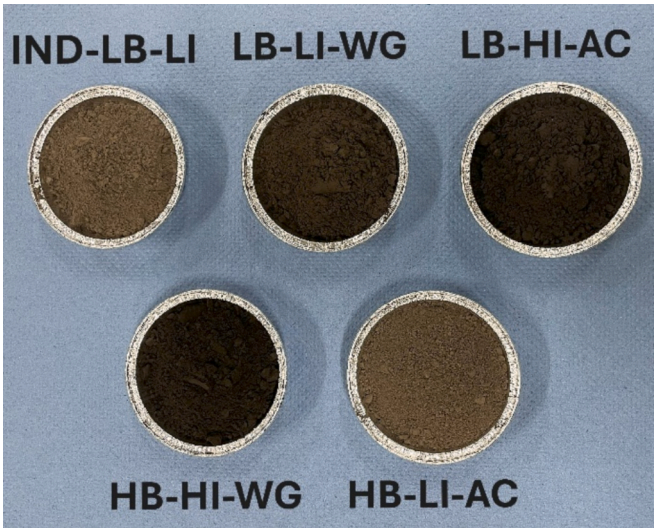

Fig. 1. Visual appearance of the investigated slags after milling.

compositions were developed in collaboration with Tata Steel to span a range of mineralogies that could plausibly arise in future DRI-fed electric arc furnaces [13,31,32]. Each composition was chosen to simulate an extreme or representative case, such as high vs. low FeO_x content or high vs. low B_2 ratio, to evaluate the distinct effects of these conditions on hydration and performance as SCMs. Additionally, two cooling regimes were employed to control the phase assemblage: water granulation to promote rapid cooling and enable the formation of amorphous phases, as well as air cooling to induce slower solidification and greater crystallinity. This design yielded four compositions: LB-LI-WG (low B_2, low iron, water-granulated), LB-HI-AC (low B_2, high iron, air-cooled), HB-HI-WG (high B_2, high iron, water-granulated), and HB-LI-AC (high B_2, low iron, air-cooled). All engineered slags were produced by melting an industrial EAF precursor slag and modifying it with mineral and oxide additions in a pilot-scale EAF. Specifically, to address leaching issues with the application, slags were doped with vanadium and chromium oxides at a 1–2 wt% level [33]. Following cooling, the slags were crushed to a particle size below 4 mm and milled to achieve a median particle size (d_{50}) comparable to that of ordinary Portland cement. The industrial EAF slag, designated IND-LB-LI, was produced through a conventional EAF steelmaking process and exhibited a similar iron content (~25 wt%) to the LB-LI-WG slag but differed in B_2, with a lower CaO/SiO_2 ratio of approximately 1.0. The reference binder used in all mixes was CEM I 52.5R, compliant with EN 197–1 [34]. A high-purity limestone filler ($CaCO_3 > 98$ wt%, $d_{50} \approx 15$ μm) was also incorporated in one sample as a reference (REF (LSF)). Standard sand, complying with EN-196 [35], was used as fine aggregate in mortar mixes, and deionized water with electrical conductivity <0.1 μS/cm was used in all mixes.

2.2. Characterization of raw materials

2.2.1. Chemical composition

The chemical compositions of the slags (Table 1) were provided by Tata Steel Netherlands and determined through a combination of X-ray fluorescence (XRF) analysis and Fe titration. XRF was conducted on fused beads prepared using lithium borate flux ($Li_2B_4O_7$:$LiBO_2$ = 65:35) in a 1:10 sample-to-borate weight ratio, following determination of loss on ignition (LOI). Analyses were performed on a PANalytical Axios spectrometer. In this context, total iron is calculated based on purely divalent iron. Fe speciation was determined separately using redox titration according to ISO 5416:2006 [36] and ISO 9035:1989 [37]. The designed variations in basicity ($B_2 \approx 1.3$ vs. ≈ 2.0) and FeO_x content (~25 vs. ~50 wt%) were closely achieved, with measured B_2 values ranging from 1.28 to 1.96. Among the engineered, LB-HI-AC shows the

Table 1
Bulk chemical compositions of slags by XRF and Fe titration.

Label	Compositions [wt%]													B_2	GOI at 950 °C
	FeO_x*	FeO** (Fe^{2+})	Fe_2O_3** (Fe^{3+})	CaO	MgO	Al_2O_3	SiO_2	MnO	TiO_2	Cr_2O_3	V_2O_5	P_2O_5	Others		
LB-LI-WG	25.2	10.8	14.4	25.8	16.3	6.0	20.1	2.0	0.9	2.3	0.9	0.7	0.05	1.28	1.2
LB-HI-AC	48.8	28.1	20.7	16.6	11.6	3.7	12.8	2.0	0.9	1.5	1.3	0.8	0.03	1.30	3.0
HB-HI-WG	39.3	29.7	9.6	26.3	10.9	3.5	13.4	2.2	1.0	1.3	1.0	0.7	0.05	1.96	3.3
HB-LI-AC	19.7	15.2	4.5	37.0	11.6	4.8	19.5	2.2	1.0	1.7	1.4	0.7	0.05	1.90	2.2
IND-LB-LI	25.7	17.8	7.9	26.6	5.1	7.2	25.1	5.4	0.4	1.9	0.1	0.4	0.09	1.06	2.4

* Total iron is calculated based on purely divalent iron.
** Determined by Fe redox titration (ISO 5416; ISO 9035) [36,37].

most substantial Fe enrichment, while HB-LI-AC attained the highest CaO content. The industrial slag (IND-LB-LI) matched the low-Fe group in iron content but exhibited a lower B_2 (≈1.06) than the engineered slag. Minor oxides include MgO (10–12 wt%), Al_2O_3 (3–5 wt%), and MnO (≈2 wt% in engineered, 5.4 wt% in the industrial slag), along with trace TiO_2, Cr_2O_3, V_2O_5, and P_2O_5. Gain on ignition (GOI) at 950 °C ranged from 1.2 to 2.4 wt% for the low-Fe slags and 3.0–3.3 wt% for the high-Fe slags. These values arise from oxidation of metallic Fe and RO-phase to higher-valence oxides (Fe_3O_4, Fe_2O_3) during heating [38,39]. The higher GOI in Fe-rich slags reflects the greater abundance of oxidation-prone phases.

2.2.2. Mineralogical composition

Quantitative X-ray diffraction (QXRD) analysis of the five slags presented in Table 2 was conducted at the Tata Steel Netherlands R&D laboratories using a PANalytical X'Pert PRO diffractometer equipped with a Co anode ($K\alpha_1$ = 1.7901 Å, $K\alpha_2$ = 1.7929 Å) and a PIXcel 3D detector. The scanning range was 10–120° 2θ, with a fixed divergence slit of 0.5° and a 0.04 rad Soller slit. Quantification of crystalline and amorphous content was achieved using the Rietveld refinement method in TOPAS 5 software [40]. It reveals systematic differences in phase composition, which are attributed to variations in slag B_2, iron content, and cooling history. The LB-LI-WG slag is mostly amorphous (~56%) with only minor crystalline phases, including merwinite (6.5%) and iron oxides (magnetite ~14%, RO-phase ~17%). In contrast, LB-HI-AC contains essentially no amorphous phase and is dominated by iron oxides (magnetite 38%, RO-phase ~26%) along with abundant kirschsteinite (~25%). HB-HI-WG is crystalline mainly (10% amorphous), dominated by RO-phase (~47%) with substantial Ca-silicates (larnite ~20%, bredigite ~9%) and minor magnetite (~6%) and perovskite contents(~2%). HB-LI-AC is fully crystalline and rich in Ca-silicates (larnite ~25%, bredigite 26%), with significant RO-phase (~29%) and magnetite (~12%), plus a small amount of perovskite (2.6%). The industrial reference IND-LB-LI exhibits higher crystallinity (~16% amorphous phase). Its primary phase is kirschsteinite (~37%), with subordinate melilite (6.5%), magnetite (12%), and RO-phase (12%).

Table 2
Quantitative phase composition of slags determined by XRD with Rietveld refinement (wt%).

Phase	LB-LI-WG	LB-HI-AC	HB-HI-WG	HB-LI-AC	IND-LB-LI
RO Phase	17.4	25.8	46.7	28.9	11.8
Magnetite	13.6	38.0	5.6	11.5	12.0
Brownmillerite	1.1	1.9	2.3	0.2	2.6
Perovskite	0.2	0.0	1.9	2.6	0.1
C2S polymorphs	1.8	1.6	20.4	24.6	2.5
Bredigite	0.4	1.6	9.3	26.0	3.1
Melilite	0.0	0.9	0.0	0.6	6.5
Kirschsteinite	0.2	24.9	0.0	0.0	37.4
Merwinite	6.5	2.7	2.2	2.8	1.6
Other	2.5	2.6	1.9	2.4	6.7
Amorphous	56.3	0.0	9.7	0.4	15.7
Total	100.0	100.0	100.0	100.0	100.0

Overall, High-B_2 slags favor Ca-rich silicates (e.g., larnite, bredigite), whereas high FeO_x contents promote iron oxides (magnetite, RO-phase). Rapid cooling (water granulation) significantly increases the amorphous fraction (as observed in LB-LI-WG and HB-HI-WG) compared to slow air cooling, indicating suppressed crystallization at high cooling rates. These trends align with the known effects of B_2, iron content, and thermal history on EAF slag phase formation [21,25,41].

2.2.3. Particle density

The density of the slag powders, determined by a helium pycnometer per ASTM D5550 [42], ranged from 3.42 to 4.02 g/cm^3 based on ten replicate measurements. Among the engineered slags, LB-HI-AC exhibited the highest density (4.02 g/cm^3), followed by HB-HI-WG (3.87 g/cm^3), HB-LI-AC (3.64 g/cm^3), and LB-LI-WG (3.49 g/cm^3). These differences correlate with their phase assemblages (Table 2). LB-HI-AC contains abundant dense iron oxides (≈38 wt% magnetite, ≈26 wt% RO-phase), which substantially increase its bulk density. Both magnetite and RO-phase are markedly denser than the Ca-rich silicates, such as larnite and bredigite [43,44]. By contrast, HB-HI-WG contains less FeO_x and more low-density Ca-silicates (larnite ~20%, bredigite ~9% in its QXRD profile), so its overall density is lower. HB-LI-AC and LB-LI-WG have still fewer heavy Fe phases; LB-LI-WG in particular has a large amorphous fraction (~56%) and minimal Ca-silicates, which further reduces its density. Although an amorphous phase is not inherently low-density in general, it has a lower density than its equivalent crystalline assemblage [45]. These experimental trends are consistent with the general observation that crystalline, Fe-rich steel slags have higher density than glassy, Ca–Si–rich ones [46]. The industrial slag (IND-LB-LI) exhibited the lowest density (3.42 g/cm^3), likely due to residual micro-porosity or a different cooling history (e.g., slower solidification) that favors lighter phases or trapped voids.

2.2.4. Particle size distribution (PSD)

The PSD after milling was determined by laser diffraction using a FRITSCH ANALYSETTE 22 NeXT in aqueous dispersion with ultrasonication for 60 s, following ISO 13320 [47]. As illustrated in Fig. 2, all slags exhibited lopsided bimodal distributions, characterized by a dominant fine peak at 2–4 μm and a smaller coarse peak at larger sizes, overall close to the typical range for SCM applications [48]. The coarse mode appeared at lower particle sizes for the water-granulated slags (LB-LI-WG, HB-HI-WG, ~13 μm) compared to the air-cooled slags (LB-HI-AC, HB-LI-AC, ~20–30 μm). This shift is consistent with the predominance of glassy phases in the granulated slags, which fracture more efficiently during milling, whereas the coarse crystalline phases in the air-cooled slags (notably magnetite and RO-phase) can hinder comminution and promote the persistence of larger fragments [49,50]. The industrial IND-LB-LI slag exhibited peaks at 3 and 20 μm, indicating a heterogeneous particle morphology resulting from non-uniform cooling during industrial processing.

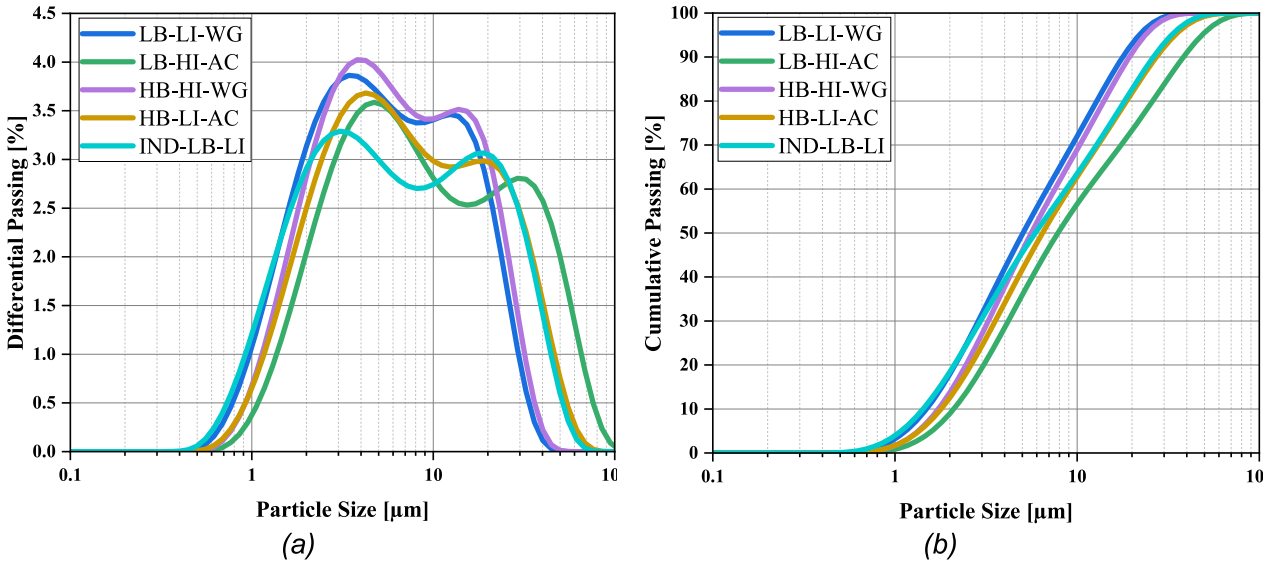

Fig. 2. (a) Differential and (b) cumulative particle size distribution curves.

3. Methods

3.1. Paste and mortar preparation

The binder systems consisted of the materials described in Section 2.1: CEM I 52.5R, four engineered slags, one industrial slag, and a high-purity limestone filler. Binary blends comprised 75 wt% CEM I and 25 wt% slag, while two control systems were used: one containing 100 wt% CEM I and another with 75 wt% CEM I and 25 wt% limestone filler, hereafter referred to as REF. Paste samples were prepared with a water-to-binder ratio (w/b) of 0.3. Mixing occurred in a planetary mixer, with 30 s of dry blending followed by 90 s after the addition of water. The fresh pastes were cast into sealed polyethylene cups for hydration. All specimens were sealed with plastic film to prevent moisture loss and carbonation and stored at 20 ± 1 °C immediately after casting. Samples were demolded at 1, 3, 7, and 28 days, and the hydration of the paste samples was stopped following the RILEM TC recommendation [51]. Mortar specimens were prepared using a binder: sand: water mass ratio of 1:3:0.5, with standard sand conforming to EN 196–1 [35] and were cast into 40 × 40 × 160 mm prismatic molds, compacted using a jolting table, sealed, and stored at 20 °C for 24 h. After demolding, the prisms were cured in saturated lime water until testing. For each mix, three replicates were cast and tested at 1, 2, 7, 21, 28, 56, and 90 days.

3.2. Test procedures

3.2.1. Heat of hydration (Isothermal Calorimetry)

Heat of hydration was measured at 20 °C using a TAM Air isothermal calorimeter per DIN EN 196–11 [52]. The calorimeter was stabilized for 24 h before testing to establish baseline conditions. For each measurement, the binder (cement plus slag or limestone) was pre-blended and then mixed with distilled water, following the procedure described in Section 3.1. The mixture was sealed and placed in the calorimeter. Reference ampoules containing distilled water were used for comparison. To ensure accurate measurements, the sample and reference ampoules were prepared with the same thermal mass, minimizing baseline fluctuations during calorimetric analysis. As per standard practice, data from the first 45 min of measurement were excluded from analysis to account for thermal equilibration and sample stabilization [53]. Heat flow was recorded continuously until the heat flow signal approached baseline. The cumulative heat release was obtained by integrating the heat flow curve. Heat flow and cumulative heat are reported per gram of total binder to enable comparison between mixes.

3.2.2. R^3 Reactivity test

The intrinsic reactivity of the slags was assessed using the R^3 (reactivity–resistance–retention) test, following the procedure described in RILEM TC-267 TRM recommendations [54]; the test results were provided by Heidelberg Materials (Benelux). Each slag was hydrated as the sole binder in a synthetic pore solution containing calcium hydroxide, potassium sulfate, and potassium hydroxide. The solution was prepared with 4.0 g L^{-1} $Ca(OH)_2$, 7.0 g L^{-1} K_2SO_4, and 0.5 mol L^{-1} KOH, and was equilibrated at 40 °C before mixing. For each test, 1.00 g of slag powder was combined with 2.00 mL of the preheated solution in a sealed ampoule and immediately placed in a TAM Air isothermal calorimeter operating at 40 ± 0.1 °C. Heat flow was recorded continuously for 7 days, and the cumulative heat release was normalized to the mass of the binder.

3.2.3. Setting evolution (Ultrasonic Pulse Velocity, UPV)

A 35 kHz ultrasonic pulse velocity (UPV) setup (IP-8, UltraTest GmbH, Achim, Germany) equipped with 40 mm diameter stainless steel probes and a fixed probe spacing of 20 mm was used to monitor the early-age hardening of paste samples non-destructively [55]. The principle of this method is that the velocity of an ultrasonic wave through the material increases as the paste stiffens, since sound propagation is directly related to the elastic stiffness of the medium [56]; UPV measurements can therefore be used as a proxy for identifying the onset and completion of setting. Following 2.5 min of mixing binder and water, the pastes were poured into cylindrical silicone molds (40 mm diameter), vibrated for 5 s to eliminate entrapped air, and covered with plastic film to minimize moisture loss. Measurements began 7 min after initial contact between the binder and water and were recorded at 1-min intervals for 7 days in a controlled room (20 ± 1 °C and 50% humidity). Monitoring was discontinued as UPV values had plateaued beyond this period, indicating structural stabilization. Coupling was ensured using ultrasound gel, and data were acquired and processed using UltraTestLab V7 software [57]. By analyzing the time derivatives of the UPV curves, inflection points corresponding to initial and final setting times were identified: the initial set was identified at the first peak of the second derivative (onset of structure formation), and the final set at the first peak of the first derivative (maximum rate of rigidity gain), consistent with established methods [58,59].

3.2.4. Drying shrinkage

Drying shrinkage was measured using a linear variable displacement transducer (LVDT). Pastes were poured into stainless steel V-shaped

molds measuring 60 mm in width, 80 mm in height, with an effective length of 100 mm. The molds were sealed with plastic film to prevent moisture loss, and axial deformation was continuously recorded at 1-min intervals over 5 days under controlled conditions (20 ± 1 °C and 50% humidity). The system had a measurement resolution of 1 μm.

3.2.5. Compressive strength

Compressive strength tests were performed on mortar prism halves after curing for 1, 2, 7, 21, 28, 56, and 90 days. Samples were loaded using a hydraulic machine at a rate of 2.4 ± 0.2 kN/s, and displacement was controlled at 1 mm/min. Results are shown as mean ± standard deviation based on six replicates. Strength activity indices (SAI) were calculated relative to the CEM I reference, with EN 450–1 limits [60] as benchmarks. All mortar strength tests were conducted by ResourceFull (Ghent, Belgium), who provided the compressive strength data used in this study.

3.2.6. X-ray diffraction (XRD)

For the hydrated paste samples, qualitative XRD analysis was performed using a Bruker D6 Advance diffractometer, equipped with Co Kα radiation (λ = 1.78897 Å), operating at 40 kV and 20 mA, on back-loaded, hydration-stopped samples mounted in a metal sample holder. Diffraction patterns were collected over a 2θ range of 5° to 90°, with a step size of 0.0207° and a scan time of 0.250 s per step. Phase determination was carried out using HighScore software [61].

3.2.7. Thermogravimetric analysis (TGA)

Thermogravimetric analysis was performed using a TG209F3 thermogravimetric analyzer (NETZSCH, Germany). Approximately 20–30 mg of hydration-stopped samples was heated from 50 °C to 950 °C at a rate of 10 °C/min under a nitrogen atmosphere with a flow rate of 50 mL/min. TG data were used to quantify portlandite and calcite by integrating mass losses in the CH dihydroxylation window (~400–500 °C) and the calcite decarbonation window (~550–750 °C), with temperature limits set from TG/DTG-guided peak positions. Phase amounts were obtained from stoichiometry (see Eqs. 1 and 2). The original, pre-carbonation portlandite was reconstructed as shown in Eq. 3. All results are reported on a 100 g anhydrous binder basis.

$$CH\ (wt\%) = \Delta m_{400°C-500°C}\frac{M_{Ca(OH)_2}}{M_{H_2O}} = 4.115(\Delta m_{400°C-500°C}) \quad (1)$$

$$CaCO_3\ (wt\%) = \Delta m_{550°C-750°C}\ \frac{M_{CaCO_3}}{M_{CO_2}} = 2.278(\Delta m_{550°C-750°C}) \quad (2)$$

$$CH_{orig}\ (wt\%) = (1) + \frac{M_{Ca(OH)_2}}{M_{CaCO_3}}\ (2) = (1) + 0.740\ (2) \quad (3)$$

3.2.8. Leaching behavior

A single-stage batch leaching test was conducted on 28-day hydrated mortars according to the procedure outlined in EN12457–2 [62]. Mortar prisms were mechanically crushed to achieve a nominal particle size below 4 mm and mixed with deionized water as the leachant at a liquid-to-solid ratio of 10 (L/Kg). Due to the limited quantity of available material, post-crushing sieving was not performed. However, all samples underwent an identical crushing protocol, and visual assessment confirmed the comparability of the resulting particle size distributions. The slurry was agitated for 24 h in a dynamic shaker (ES-SM-30, Edmund Bühler GmbH) at 250 rpm. Following agitation, the eluate was filtered through a 5 μm pore size paper filter, and the pH was measured using a Voltkraft PH-100ATC pH electrode. A portion of the filtered eluate was further filtered through a 0.22 μm (Whatman) syringe filter and acidified with ultrapure nitric acid (HNO_3). Elemental concentrations within the acidified solution were determined using inductively coupled plasma optical emission spectrometry (ICP-OES) with a Spectroblue instrument (Kleve, Germany), following the methodology described in NEN 6966 [63]. The results were subsequently compared with the regulatory limits stipulated by the Dutch Soil Quality Decree (DSQD) [64]. A complementary analysis of ionic species (Ca^{2+} and SO_4^{2-}) was performed using ion chromatography (IC), following dilution of the eluate with Milli-Q water by a factor of 20.

4. Results and discussion

4.1. SCM reactivity

The early hydration kinetics were investigated using isothermal calorimetry at 20 °C, with both heat flow and cumulative heat release profiles presented in Fig. 3. As expected, the CEM I paste displayed the highest hydration peak (~4.3 mW g^{-1}) at around 12 h, indicating rapid alite dissolution, C–S–H formation, and portlandite precipitation. The REF system, containing 25 wt% limestone filler, showed a slightly lower peak (~3.3 mW g^{-1}) at a similar time, which reflects the reduced clinker content in the blend and the associated dilution of the reactive phase fraction. Importantly, all slag mixes reached their maximum heat flow at approximately the same time (~12 h), indicating no acceleration or retardation. Among the slag-containing binders, LB-LI-WG exhibited both the highest heat flow (~3.3 mW g^{-1}) and cumulative heat release, closely matching REF in hydration intensity. This performance coincides with a high amorphous content that is likely pozzolanic. Such a highly disordered glassy network is known to promote reactivity, as its depolymerized silicate structure is particularly prone to hydrolysis [19,65]. LB-HI-AC and HB-HI-WG exhibited similar heat release, both slightly lower than that of the highly amorphous LB-LI-WG. These two high-Fe slags share a significant fraction of inert oxides, which likely limited their overall reactivity. It remains uncertain whether the crystalline phases present in LB-HI-AC and HB-HI-WG, such as kirschsteinite, larnite, and bredigite, contributed significantly to the observed reactions. The high-B_2, low-Fe slag HB-LI-AC and the industrial IND-LB-LI displayed the lowest reactivity, with HB-LI-AC showing moderate heat release and IND-LB-LI consistently recording the lowest peak (~2.0 mW g^{-1}) and cumulative heat.

4.2. Pozzolanic reactivity

The R^3 reactivity test results are illustrated in Fig. 4. LB-LI-WG was by far the most reactive, with cumulative heat exceeding 230 J g^{-1} after seven days, which coincides with its high amorphous fraction (56%). Here, "high amorphous content" refers to a relative increase compared to the corresponding air-cooled slag, rather than an absolute comparison. In contrast, the fully crystalline LB-HI-AC released around 60 J g^{-1}, confirming its near-inert character. The high-B_2 slags showed moderate reactivity, with HB-HI-WG and HB-LI-AC both releasing about 90–100 J g^{-1}, similar to the industrial IND-LB-LI slag. We note that the HB-HI-WG signal displayed a slightly unusual baseline trend, confirmed across replicate runs. While the exact cause is not fully understood, all testing protocols were strictly followed, and the behavior was reproducible. Nevertheless, these values remain significantly lower than those of conventional SCMs, with RILEM TC 267-TRM reporting 7-day R^3 cumulative heats of 160–360 J g^{-1} for fly ash, 250–960 J g^{-1} for calcined clays, and 350–550 J g^{-1} for GGBFS [54]. Taken together, these findings indicate that the cooling regime, through its control of amorphous formation, is the dominant factor governing the reactivity of the investigated slags. In contrast, Fe content and B_2 exert only a secondary influence. This interpretation is consistent with the isothermal calorimetry of cement–slag blends, where LB-LI-WG produced the highest heat release and promoted faster hydration, while crystalline slags showed subdued calorimetric signatures.

4.3. Setting and hardening evolution

Fig. 5 shows the UPV results: (a) velocity–time curves, (b) first

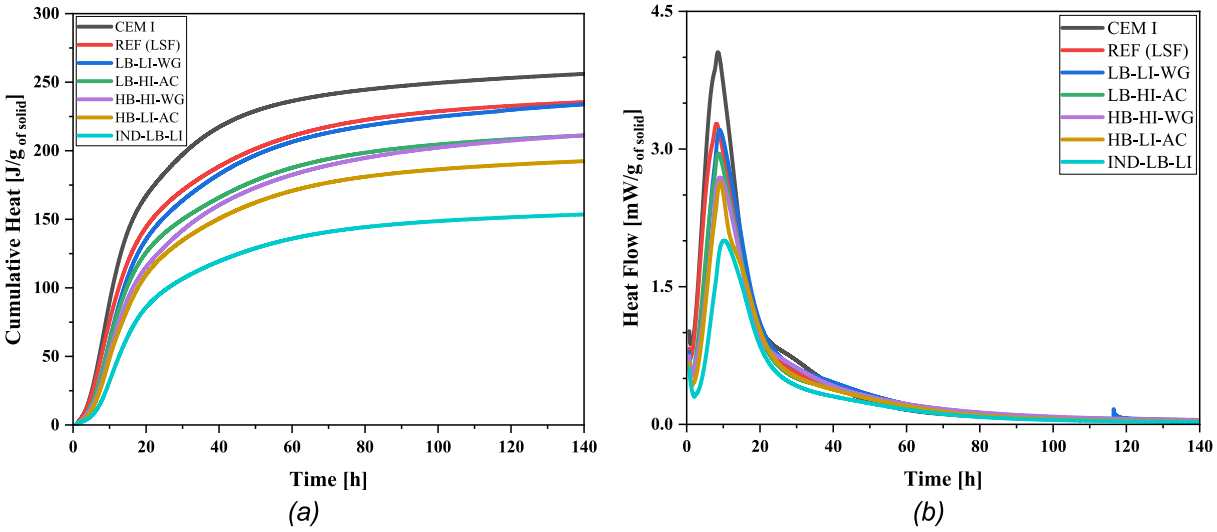

Fig. 3. Isothermal calorimetry: (a) Cumulative heat release and (b) heat flow.

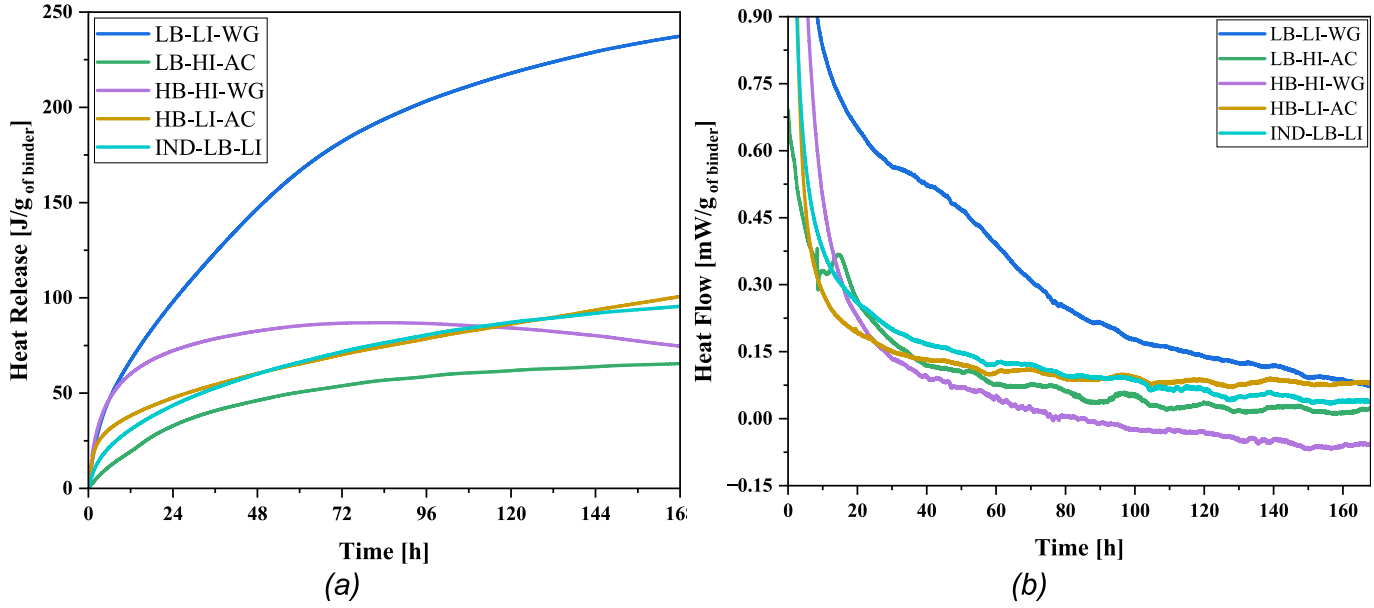

Fig. 4. R3 Test: (a) Cumulative heat, (b) Heat flow.

derivative, (c) second derivative, and (d) the derived setting times. The initial set (Fig. 5c) shows that the earliest peaks occur for CEM I and REF (25% limestone), followed by the low-B_2 slag blends, then HB-LI-AC and HB-HI-WG, and lastly the IND blend. In absolute terms, CEM I reached the initial set at ~47 min and REF at ~51 min; the slag-bearing blends occurred later, with IND being the latest at ~115 min. Given that the binder still contains 75 wt% CEM I, these shifts represent perturbations of the cement-dominated setting trajectory. As shown in (Fig. 5d), REF reached the final set at ~62 min and CEM I at ~87 min; the HB slag blends followed (typically ~120 min), then the LB blends (~140–150 min), and IND last at ~200 min. This hierarchy is consistent with Section 4.1: blends with lower cumulative hydration heat at early age set later, whereas the limestone reference achieves an earlier final set than CEM I, despite lower total heat, owing to its well-known nucleation/filler effect that accelerates alite hydration and network formation per unit time of reaction [66–68]. The apparent absence of a clear delay in the calorimetric peak time for the slag blends despite their delayed UPV-derived setting can be rationalized by the different sensitivities of the two methods: isothermal calorimetry records heat release (dominated by clinker reactions at early age) and thus its peak timing is governed mainly by alite kinetics, which are only modestly affected at 25% replacement; UPV, in contrast, reflects the emergence of a continuous, load-bearing hydrate skeleton and therefore depends on the rate of volume generation of hydrates and their connectivity. With 25 wt% of the binder replaced by low-reactive slag, the volumetric production of hydrates per unit time is reduced (dilution plus lower slag contribution), so the percolation threshold is reached later, even if the calorimetric peak time does not shift substantially. Compositionally, the earlier final set of the HB systems relative to LB (HB < ~120 min vs LB ~ 140–150 min) aligns with the QXRD-indicated presence of Ca-rich silicates (larnite/bredigite) in HB slags, which supply Ca^{2+} and promote faster consolidation once hydration is underway; conversely, the IND blend, dominated by slowly dissolving kirschsteinite and with limited amorphous content, shows the latest set.

4.4. Drying shrinkage

Fig. 6 illustrates the drying shrinkage of paste systems over 5 days.

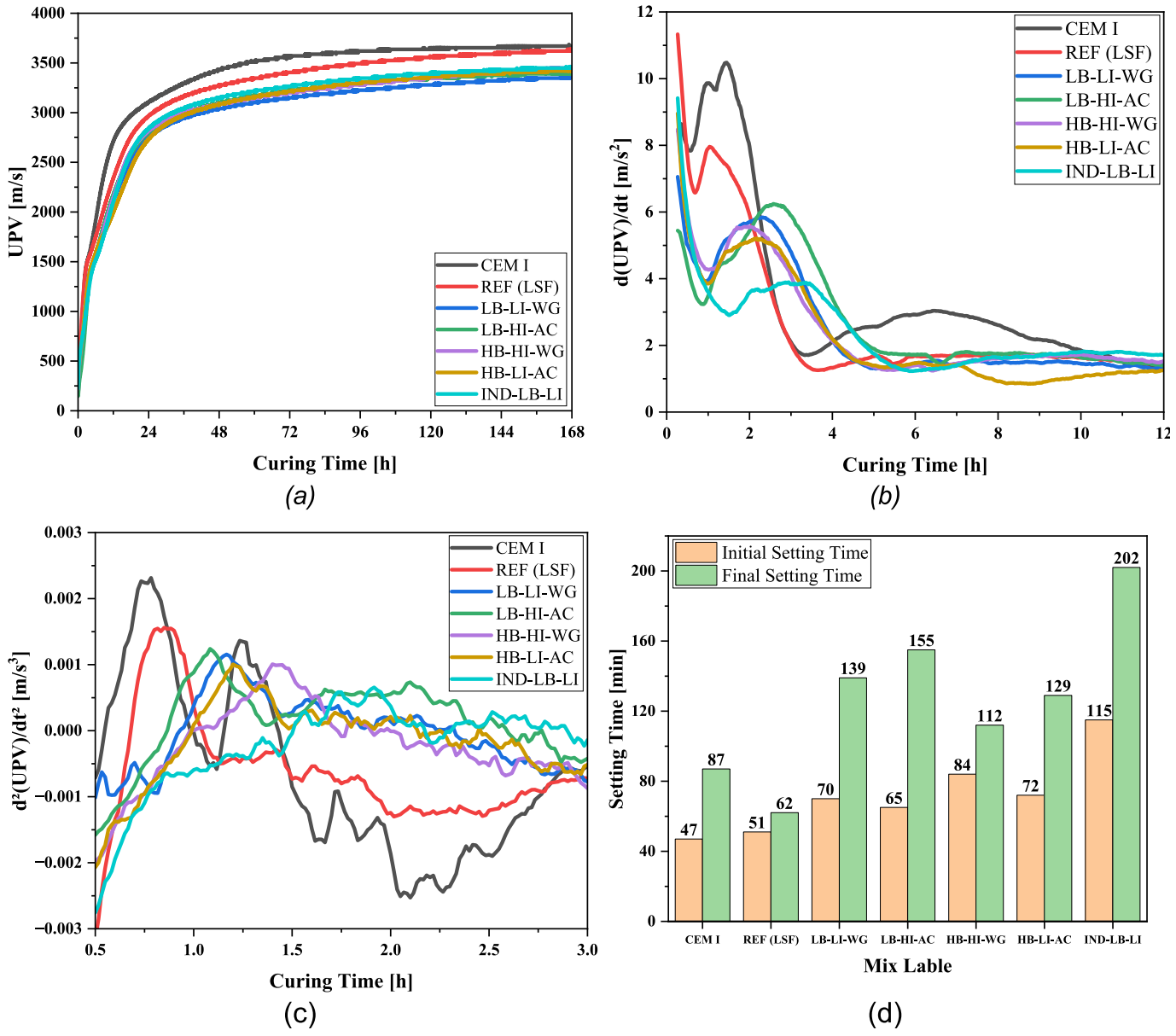

Fig. 5. (a) UPV evolution; (b) first and (c) second derivatives used to identify final and initial setting times, respectively; (d) derived setting times for paste systems.

Incorporating 25 wt% limestone in the REF mix mitigated shrinkage, likely due to its filler effect and influence on internal curing [67]. The low-B_2 slag blends (LB-LI-WG and LB-HI-AC) exhibited shrinkage trajectories that were nearly indistinguishable from the CEM I. If the replacement were purely inert, a 25% clinker reduction would typically lower drying shrinkage. The fact that shrinkage remains comparable to CEM I indicates that these low-B_2 slags contribute to early hydrate formation and pore refinement, sustaining capillary stresses that offset dilution, consistent with capillary-pressure control of drying shrinkage [69,70]. In contrast, the high-B_2 slag blends (HB-HI-WG and HB-LI-AC) formed a distinct intermediate group, with shrinkage rates consistently greater than the REF blend but lower than those of CEM I and the low-B_2 systems. This aligns with their lower early cumulative heat (Section 4.1): reduced early reactivity produces slower pore refinement and thus lower capillary tension per unit time, resulting in intermediate shrinkage despite the identical 25% replacement. The industrial slag (IND-LB-LI) aligned closely with the high-B_2 group, displaying shrinkage values comparable to those of HB-HI-WG and HB-LI-AC. This convergence is noteworthy, as IND-LB-LI differs from the engineered slags in both chemistry and cooling history; yet, its shrinkage performance nevertheless parallels that of the high-B_2 compositions.

4.5. Mechanical performance

4.5.1. Mortar compressive strength

As shown in Fig. 7a, all mortar mixtures exhibit a steady increase in compressive strength with age up to 90 days. The CEM I control maintains the highest strength at each interval, reaching approximately 65 MPa by 90 days. Among the slag-substituted mortars, the water-granulated slags consistently outperformed their air-cooled counterparts. By 28 days, the water-granulated blends attained compressive strengths of ~50–55 MPa, whereas the air-cooled mixes reached only ~40–45 MPa. This trend persisted at later ages: at 56 days, the water-granulated slag mortars exceeded 55 MPa, while the air-cooled mixes remained in the upper 40s MPa range. By 90 days, water-granulated mixes achieved ~60 MPa, whereas air-cooled slags plateaued around 50–53 MPa. The industrial slag blend (IND-LB-LI) followed a similar trend: despite a slower initial hydration rate, it developed ~45 MPa by

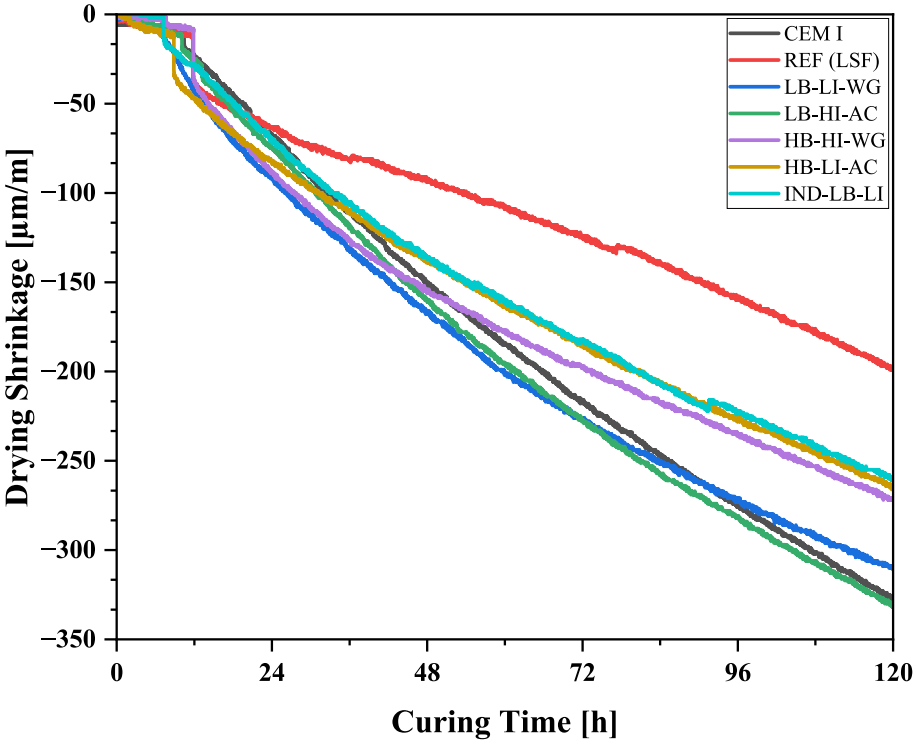

Fig. 6. Drying shrinkage of slag-cement pastes during the first 120 h.

28 days. It continued to gain strength, reaching 53 MPa at 90 days, which is comparable to that of engineered air-cooled slag mortars. This prolonged strength development in IND-LB-LI suggests that extended hydration (or secondary reactions) can partially compensate for its initially low reactivity, likely associated with slow hydration of Ca-silicates (kirschsteinite-rich with minor β-C_2S). High-B_2 EAF slags, with greater CaO content, are generally expected to promote the formation of calcium-rich hydrates (e.g., C–S–H), which enhance microstructural densification and load-bearing capacity [71]. However, in this study, the high–low B_2 strength gap is modest. Blends with similar reactive Ca-silicate inventories (amorphous + bredigite/β-C_2S) reach comparable strengths regardless of bulk B_2. Iron phases are secondary: higher-Fe mixes may gain slightly early via Kirschsteinite dissolution, whereas magnetite is inert, and the RO-phase is weakly reactive; they do not sustain later strength. Long-term performance tracks cooling-controlled amorphous content and reactive Ca-silicates rather than bulk Fe.

4.5.2. Strength activity index

Fig. 7b presents the strength activity index (SAI) for the slag-containing mortars, defined as the percentage of the CEM I control strength achieved by the 25% slag blend at equal ages. This metric highlights the evolution of slag reactivity relative to the pure cement benchmark. The REF blend exhibited the lowest SAI, highlighting the limited mechanical contribution of limestone. All slag mixes exhibited low initial reactivity (SAI well below 65% at 2 days), but their indices increased substantially over time as slag hydration progressed. By 28 days, every slag blend comfortably exceeded the 70% minimum SAI specified by EN 450–1 and therefore at least fulfils the strength specification for fillers in the Netherlands [72]. The water-granulated slags (LB-LI-WG and HB-HI-WG) demonstrated the highest reactivity, reaching ~85–90% of the control strength by 28 days, essentially meeting the 90-day benchmark early. The air-cooled mixes lagged slightly behind their water-granulated counterparts at 28 days (SAIs ~75–80%), but still surpassed the minimum threshold. By 90 days, continued hydration improved the SAI of the air-cooled mixes; however, LB-HI-AC remained below the 80% requirement, highlighting the lower long-term reactivity of air-cooled crystalline slags compared to water-granulated counterparts, especially when B_2, glass, and Ca-rich phase content are limited. As B_2, cooling history, and Fe content primarily manifest through their control on mineralogy, the iron contribution appears secondary in the present study once mineralogy is considered. Fe is partitioned mainly into magnetite/RO-phase (inert–weakly reactive) and kirschsteinite (partially reactive), whereas SAI at 28–90 days is governed by the amorphous phase and Ca-rich silicates (bredigite, β-C_2S, merwinite/melilite). Consequently, despite higher Fe, HB-HI-WG attains a 90-day SAI comparable to LB-LI-WG (~90%). The water-granulated slags outperformed their air-cooled counterparts, but not in the same way. LB-LI-WG, with its high amorphous fraction, showed rapid early strength development, whereas HB-HI-WG, despite having less amorphous content, benefited from its higher CaO content and more reactive Ca-silicates.

4.6. Phase evolution

4.6.1. XRD

X-ray diffractograms collected at 1, 3, 7, and 28 days (Fig. 8) reveal the fate of the original slag minerals and the evolution of cement hydration products in the blends. As summarized in Table 2, the dominant crystalline phases in the starting slags include kirschsteinite in the low-B_2 systems (LB series and IND), bredigite and larnite in the high-B_2 slags (HB series), and RO-phase/magnetite in the high-iron slags. These starting assemblages serve as a reference point for evaluating the extent to which individual slag phases persist or react during hydration.

Kirschsteinite is prominent in the low-B_2 systems (Fig. 8a, b, and e). Its strongest reflection near ~26° 2θ is weak in LB-LI-WG (trace in the raw slag) and remains barely detectable at all ages; in LB-HI-AC and IND-LB-LI, it is more visible at 1–7 days and shows reduced intensity by 28 days, supporting that kirschsteinite participates in the hydration process. Notably, published data on kirschsteinite reactivity in cementitious media are limited. For bredigite, characteristic of the high-B_2 slags (HB-LI-AC, HB-HI-WG), no systematic consumption is visible over 28 days, consistent with its low early reactivity in alkaline pore solution

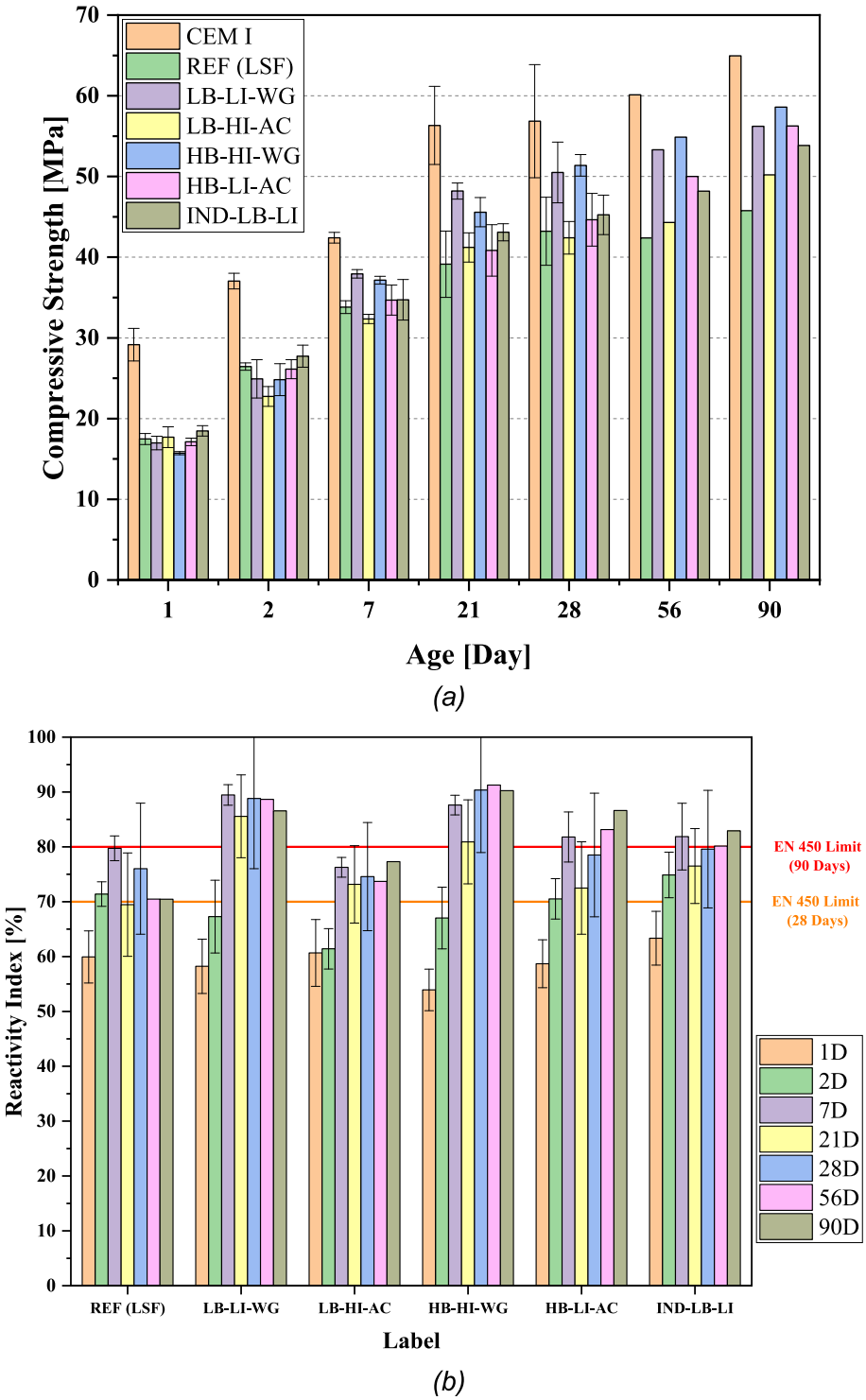

Fig. 7. Compressive strength development: (a) evolution over time; (b) Strength Activity Index.

(slower than slag's amorphous content and belite) [73,74]. Fe-rich phases magnetite and RO show markedly sharper, more intense reflections in the high-iron systems (LB-HI-AC, HB-HI-WG; Fig. 8c, d) primarily because their modal abundance is higher. Their peak intensities and positions remain essentially unchanged from 1 to 28 days, consistent with the low reactivity commonly reported for these phase [75]. Larnite overlaps with clinker peaks and cannot be assessed independently in these patterns.

The cement phase, Brownmillerite C2(A,F), is most prominent in the 1-day-old samples and is rapidly consumed between 1 and 7 days. Ettringite (AFt) is visible in all samples and only begins to show a slight decrease at 28 days. Portlandite ($Ca(OH)_2$) was also observed in all mixes, arising primarily from clinker hydration and increasing over time in all samples. Kuzelite-type monosulfate was visible at 28 days. Quartz and dolomite were only present in minor amounts, but could still be distinguished in several patterns. In the engineered mixes, these peaks originate solely from the cement component, while in the industrial slag, they derive from both the cement and the slag itself. Their intensity remained essentially unchanged during hydration, consistent with their inert character under the curing conditions used [68]. A weak but

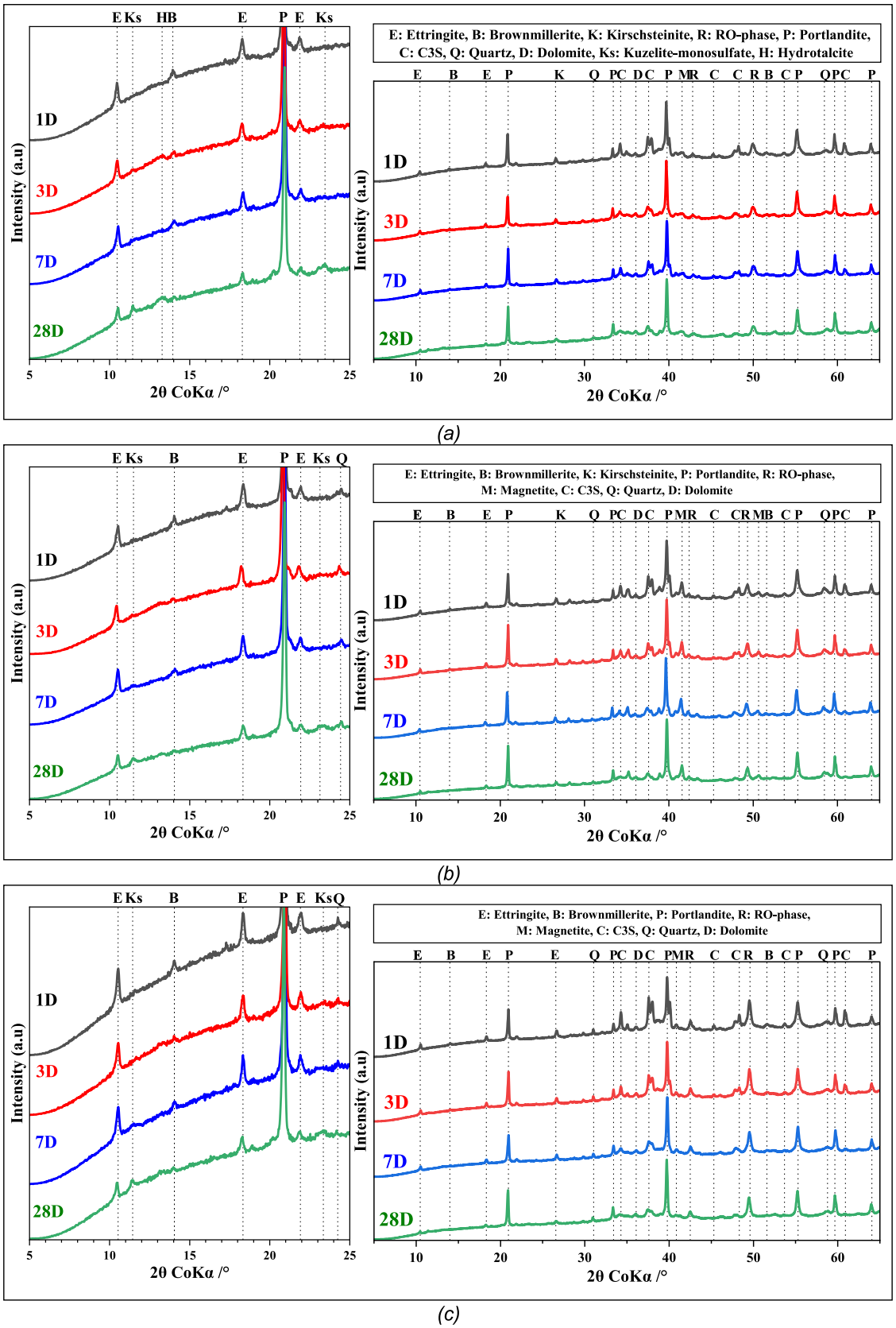

Fig. 8. XRD patterns of hydrated slag–cement pastes at 1, 3, 7, and 28 days: (a) LB-LI-WG, (b) LB-HI-AC, (c) HB-HI-WG, (d) HB-LI-AC, (e) IND-LB-LI, and (f) comparison of all systems at 28 days.

discernible shoulder around 11° 2θ developed between 3 and 7 days in LB-LI-WG and intensified by 28 days, indicating the formation of LDHs.

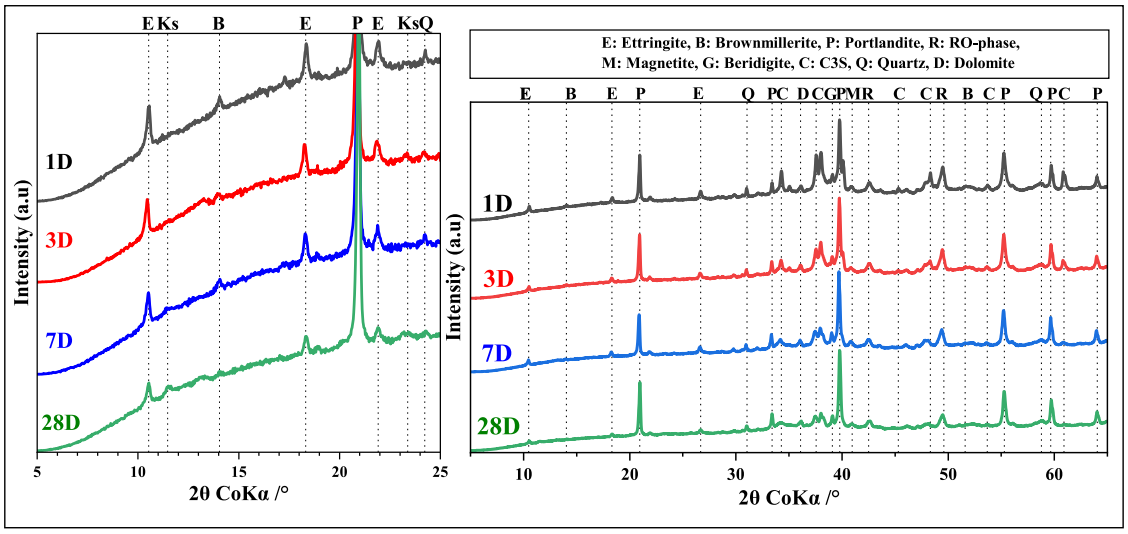

(d)

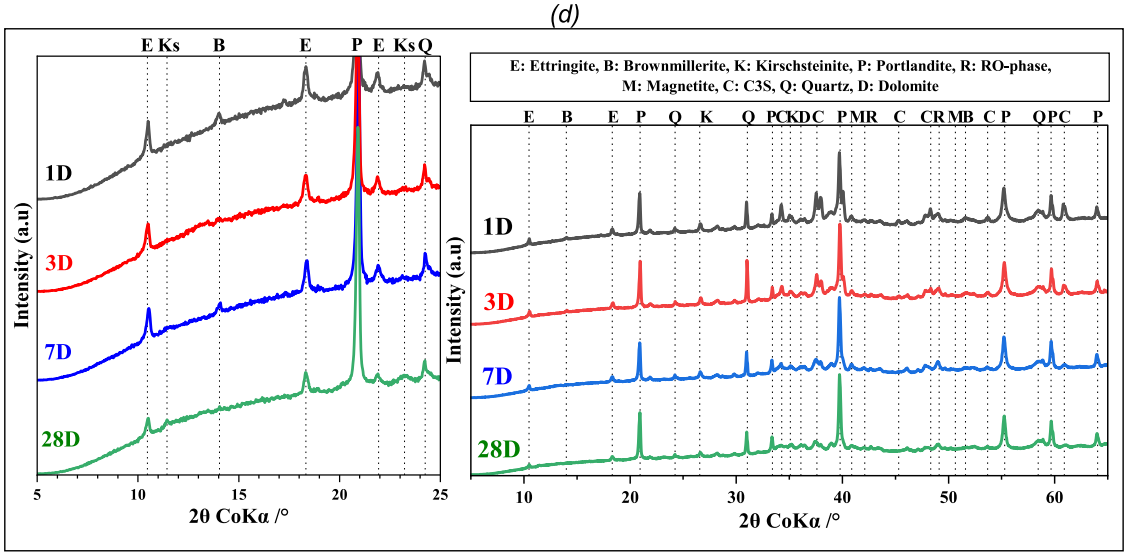

(e)

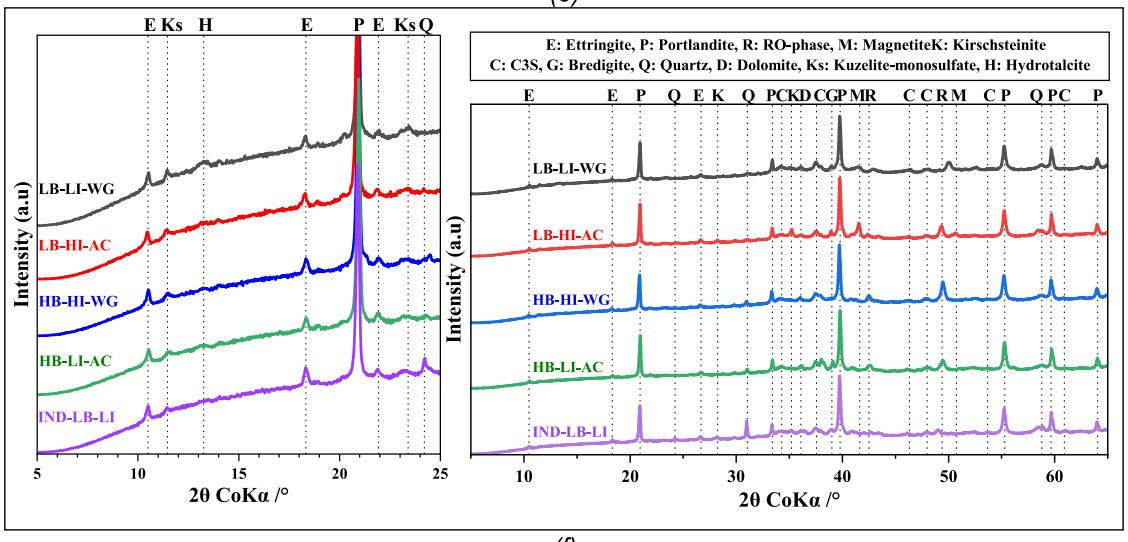

(f)

Fig. 8. (*continued*).

These LDHs are hydrotalcite-like Mg—Al layered double hydroxides, with a brucite-type structure of Mg^{2+}/Al^{3+} hydroxide layers and interlayer anions (mainly CO_3^{2-}) plus water [68,69]. Their formation is strongly dependent on Mg availability, which explains the clearer signal in LB-LI-WG. In the other engineered slag systems, LDH reflections were absent or negligible, reflecting their lower Mg availability (See Table 1).

This observation is further corroborated by the TG results (see Section 4.6.2).

4.6.2. TGA

Thermogravimetric and derivative thermogravimetric curves (Fig. 9) were collected for all slag–cement pastes at 1, 3, 7, and 28 days. The principal mass-loss regions correspond to dehydration of C–S–H and AFt/AFm below ~200 °C, LDH dehydroxylation at ~330–400 °C, Ca(OH)$_2$ dehydroxylation at ~400–500 °C, and decarbonation of carbonates at high temperature (limits DTG-guided). To enable quantitative comparison, portlandite (P), calcite (C), and the back-calculated original portlandite (OP) are reported in Table 3.

The general shape of the curves is similar for all systems, since hydrated cement constitutes 75% of the mixes. Still, the relative intensities and temporal evolution of the peaks vary with slag chemistry and cooling history. In all binders, the mass loss peak associated with Aft/AFm decomposition appears already at 1 day, centered at ~100 °C. For LB-LI-WG and LB-HI-AC (Fig. 9a, b), the peak height at 100 °C remains essentially constant over the testing ages. In IND-LB-LI (Fig. 9e), a slight shift of the peak maximum toward higher temperature is observed, whereas the other systems show no significant change. A low-temperature shoulder near ~75 °C was observed at early ages and disappeared by 3 days, plausibly reflecting partial dehydration of nascent ettringite (AFt) and/or very loosely bound water in early C–S–H.

Carbonate-corrected original portlandite (OP) increased with age in all binders, reflecting continued clinker hydration during the first month. At 28 days, OP ranged from 20.9 wt% (LB-LI-WG) to 23.4 wt% (IND-LB-LI). Air-cooled slags, which are more crystalline and low in amorphous phase, retain higher OP because the limited amorphous content reduces CH uptake into secondary hydrates. Water-granulated slags, richer in amorphous phase and thus more reactive, show lower OP due to faster incorporation of CH into C-(A)-S-H. Nonetheless, the upward trend is consistent across all plots, underscoring that slag replacement at 25 wt% does not deplete CH within the first month.

Carbonate losses (C) varied by mix and age, indicating that part of the CH formed subsequently carbonated during curing/handling. Recalculating the calcium carbonate formed in CH yields OP, which more accurately reflects the CH produced by hydration. OP at 28 days scales with amorphous fraction and crystalline Ca-silicate abundance: IND-LB-LI (23.4 wt%) and HB-LI-AC (23.2 wt%) exhibit the highest CH production, followed by LB-HI-AC (22.4 wt%), HB-HI-WG (21.6 wt%), and LB-LI-WG (20.9 wt%). This ranking aligns with QXRD, where the mixes richer in β-C$_2$S/bredigite (IND-LB-LI, HB-LI-AC) generate more CH over 28 days, while amorphous-rich systems (e.g., LB-LI-WG, HB-HI-WG) display lower measured CH because a larger fraction is consumed in secondary C-(A)-S-H formation; their OP values remain comparable, indicating substantial underlying CH production despite lower residual CH.

Minor shoulders in the 330–400 °C range, most prominently observed in the LB-LI-WG paste, indicate the formation of LDHs. In the other slag systems, these features are very weak or nearly absent. By 28 days, the DTG patterns of all systems are almost identical (Fig. 9f), indicating convergence of the hydrate assemblage over time.

4.7. Leaching

Table 4 shows the elemental leaching of the mortars. All formulations fully complied with the DSQD [64] target values for unbound construction materials. Leached amounts of the potentially toxic elements barium, chromium, molybdenum, and vanadium were well below their respective limits. Barium showed the highest release among these species, ranging from 8.37 to 13.16 mg kg^{-1}, which is at most ~60% of the 22 mg kg^{-1} DSQD limit. The Ba budget is dominated by the cementitious matrix rather than by the slag, as reflected by similar Ba release in the CEM I/REF and the slag blends, consistent with Ba originating from Portland cement [76]. Importantly, the industrial slag (IND-LB-LI) is essentially vanadium-oxide free, whereas the four engineered slags were intentionally V-doped at ~1 wt% (bulk), yet this compositional difference did not translate into higher V leaching; V remained at or below trace levels in all binders. Non-regulated elements like aluminum and iron were similarly low in the leachates (Al ≈ 1 mg kg^{-1}, Fe < 0.1 mg kg^{-1}), indicating their incorporation into insoluble hydration products [77]. The eluates remained strongly alkaline (pH 12.7–12.9), consistent with Ca(OH)$_2$-saturated pore solutions and sustained alkalinity buffering by the slag–cement system, in line with the elevated Ca release. Under these high-pH conditions, many metal species are sparingly soluble. For example, oxyanions like CrO_4^{2-} and VO_4^{3-} have a limited affinity for ordinary C–S–H at pH levels above 12, but secondary phases can immobilize them. Iron leaching was also negligible, as any Fe^{2+}/Fe^{3+} released would rapidly form insoluble Fe(OH)$_3$ or be taken up by LDH-type phases. Overall, the influence of slag chemistry (B$_2$ or Fe content) and cooling history on leaching behavior was secondary compared to the influence of the PC. Still, some trends were observed. The water-granulated slags tended to exhibit a higher release of Mo and V than their air-cooled counterparts, likely due to the reactivity of the amorphous phase formed during rapid cooling. The air-cooled slags, being more crystalline, hydrated more slowly and generally released even smaller amounts of trace elements. The overall leaching of heavy metals from the slag-blended mortars closely matched that of a CEM I control, underscoring that replacing 25% of cement with engineered EAF slag did not compromise environmental performance.

5. Conclusion

This study evaluated the hydration, mechanical, and environmental performance of engineered DRI–EAF slags representing future fossil-free steelmaking residues. By systematically varying basicity, Fe content, and cooling regime in a controlled matrix, the work offers a rare multivariate perspective that clarifies how these interrelated parameters affect the reactivity as supplementary cementitious materials at 25 wt% substitution of Portland cement.

Slag chemistry set the mineralogical baseline. Higher basicity favored Ca-rich silicates such as larnite and bredigite, whereas elevated Fe stabilized RO-phase/magnetite. Superimposed on this compositional control, the cooling regime determined the amorphous fraction. Although water granulation increased glass content relative to air cooling, the absolute amorphous fraction remained modest. This is attributed to the early crystallization of Fe-rich phases, such as the RO solid solution, at high temperatures, which limited the extent of amorphous formation even under rapid cooling. These findings highlight that the cooling rate, rather than slag chemistry alone, is the primary determinant of amorphous-forming ability and, consequently, reactivity as an SCM.

R^3 tests showed that slags richer in amorphous and readily hydrating Ca-silicates were intrinsically more reactive, whereas Fe-rich systems with Fe partitioned into RO/magnetite were less reactive.

SCM reactivity revealed that differences in kinetics primarily arose from the magnitude rather than the timing: the central hydration peak remained near 12 h for all binders (alite-dominated). In contrast, peak height and cumulative heat followed the availability of the reactive phase. Mechanical results showed that all slag mortars exceeded the EN 450–1 requirement of 70% relative strength at 28 days. Water-granulated slags reached ~60 MPa by 90 days, approaching the strength of pure cement controls, while air-cooled slags plateaued near 50 MPa.

Across all binders, hydrate assemblages converged toward C–S–H, ettringite, and portlandite, with monosulfate stabilizing by 28 days. Hydrotalcite-like LDHs were observed in a low-basicity water-granulated system, as confirmed by calorimetry, TGA, and XRD, indicating that chemistry and cooling jointly regulate phase evolution.

Leaching tests verified environmental safety, with all trace element concentrations far below Dutch Soil Quality Decree thresholds. The LDH

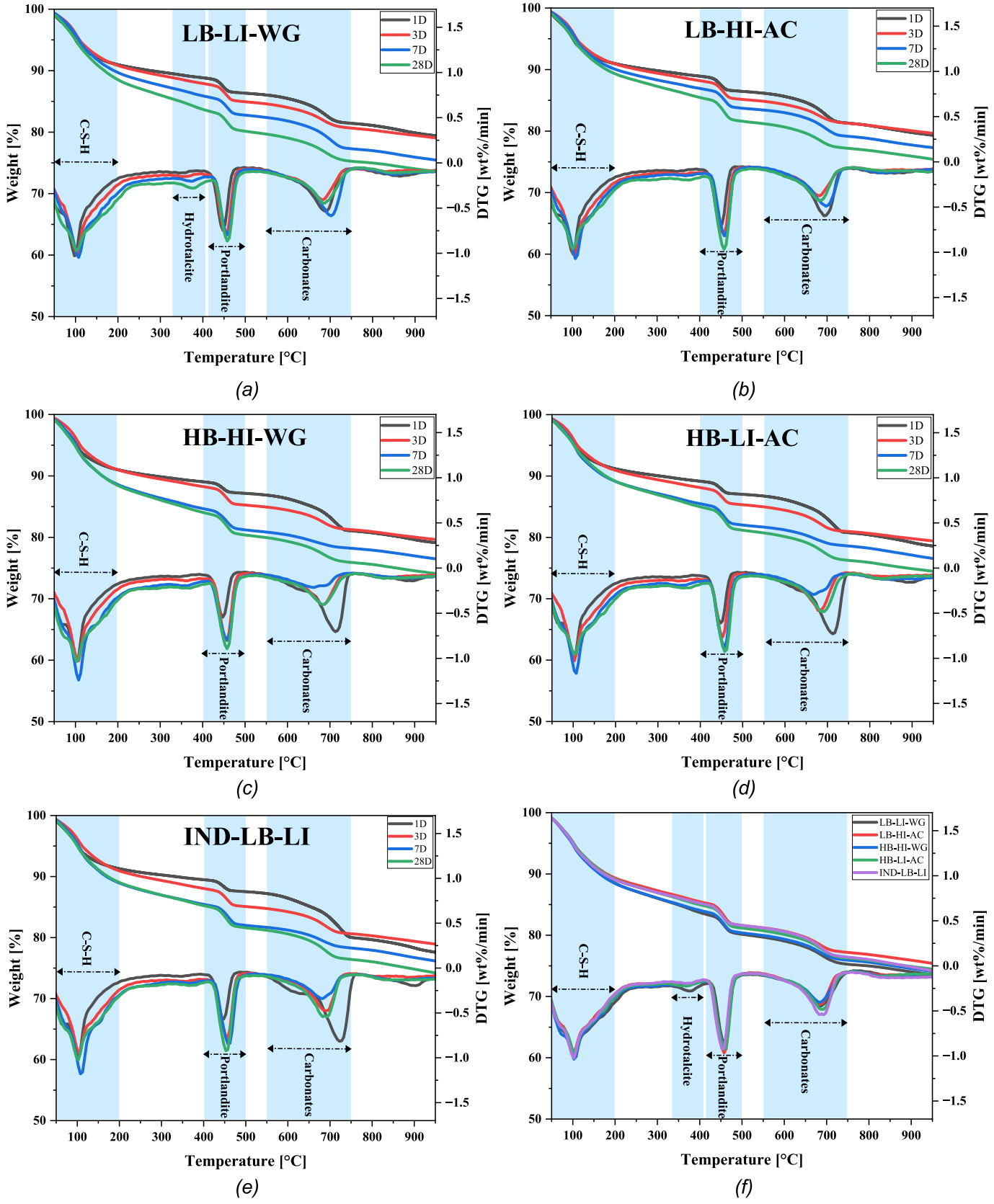

Fig. 9. TG/DTG curves of hydrated slag-cement systems at 1, 3, 7, and 28 days: (a) LB-LI-WG, (b) LB-HI-AC, (c) HB-HI-WG, (d) HB-LI-AC, (e) IND-LB-LI, and (f) comparison of all systems at 28 days.

Table 3
Back-calculated original portlandite content (wt%, per 100 g anhydrous binder) from TG/DTG-guided windows.

Age (Day)	Mix label														
	LB-LI-WG			LB-HI-AC			HB-HI-WG			HB-LI-AC			IND-LB-LI		
	P*	C**	OP***	P	C	OP	P	C	OP	P	C	OP	P	C	OP
1	9.8	10.5	17.6	10.1	11.1	18.3	7.8	13.2	17.6	8.8	13.1	18.6	8.0	16.4	20.1
3	11.7	8.9	18.2	12.4	8.1	18.4	12.3	8.3	18.4	11.3	9.1	18.0	12.0	9.3	18.9
7	12.2	11.5	20.7	13.0	9.7	20.2	14.0	5.9	18.4	14.4	6.9	19.6	14.0	8.5	20.2
28	13.5	10.0	20.9	15.7	9.0	22.4	14.9	9.1	21.6	15.8	10.1	23.2	14.7	11.8	23.4

* Calculated portlandite by (Eq. 1).
** Calculated calcite by (Eq. 2).
*** Back-calculated original portlandite by (Eq. 3).

Table 4
Element concentrations in mortar leachates (mg kg^{-1}, ICP-OES/IC) with Dutch soil quality decree (DSQD) [64] reference limits.

ID	pH	Al	Ba	Cr	Fe	Mg	Mo	V	Si	Ca^{2+}	SO_4^{2-}
DSQD Limit	N.A	–	22	0.63	–	–	1	1.8	–	–	2430
CEM I	12.81	1.47	9.68	0.04	0.06	0.61	0.01	0.01	4.76	6386.44	23.19
REF (LSF)	12.83	0.85	8.04	0.10	0.05	0.84	0.03	0.01	3.80	6081.56	28.75
LB-LI-WG	12.83	1.56	8.60	0.04	0.02	0.66	0.07	0.03	5.88	6212.31	25.83
LB-HI-AC	12.83	1.45	9.53	0.08	0.03	0.03	0.04	0.00	3.30	6550.85	23.08
HB-HI-WG	12.78	0.85	8.37	0.04	0.03	0.57	0.07	0.00	4.77	5812.64	28.43
HB-LI-AC	12.86	1.17	9.95	0.05	0.01	0.07	0.02	0.00	4.07	6734.81	25.15
IND-LB-LI	12.83	1.43	13.16	0.06	0.02	0.05	0.04	0.00	3.46	6588.25	22.89

and AFm phases facilitated the effective immobilization of Cr, V, and Mo under strongly alkaline conditions.

These findings confirm that water granulation, as a form of rapid cooling compared to air cooling, substantially increases the amorphous content and enhances reactivity in DRI–EAF slags. A potentially fine microstructure or amorphous material governs the positive synergy with CEM I, while basicity and Fe content fine-tune hydration kinetics and dimensional stability. Although the fine particle size and low replacement level reduce the risk of RO-phase expansion in this study, long-term effects remain under investigation and warrant further microstructural analysis of the used slags. These findings provide design principles for valorizing steel slags from low-CO2 steel-making processes as sustainable binders in low (CO_2)footprint cementitious systems.

CRediT authorship contribution statement

Morteza Tayebi: Writing – review & editing, Writing – original draft, Visualization, Validation, Software, Methodology, Investigation, Formal analysis, Data curation, Conceptualization. **Katrin Schollbach:** Writing – review & editing, Validation, Supervision, Resources, Project administration, Methodology, Funding acquisition, Conceptualization. **J.C.O. Zepper:** Writing – review & editing, Resources, Project administration, Methodology, Funding acquisition, Conceptualization. **Stefan Melzer:** Writing – review & editing, Software, Formal analysis, Data curation. **H.J.H. Brouwers:** Writing – review & editing, Validation, Supervision, Project administration, Methodology, Conceptualization.

Declaration of competing interest

The authors declare that they have no known competing financial interests or personal relationships that could have appeared to influence the work reported in this paper.

Acknowledgements

This research was conducted under project number T23006b within the framework of the Research Program of the Materials Innovation Institute (M2i) (www.m2i.nl), supported by the Dutch government. The authors would like to acknowledge the following sponsors of this research: Tata Steel Netherlands, Heidelberg Materials, Ecocem, and Pelt & Hooykaas. Here, also the effort of Institut für Baustoff-Forschung e.V (FEhS) and Bundesanstalt für Materialforschung und-prüfung (BAM) is acknowledged for producing the engineered slags to the desired target compositions. Moreover, the authors would like to express their appreciation to the ResourceFull (Ghent, Belgium) company for producing and mechanically testing mortar prisms. In addition, the authors appreciate Anneke Delsing's help with the ICP and IC measurements.

Data availability

Data will be made available on request.

References

[1] T. Watari, A. Cabrera Serrenho, L. Gast, J. Cullen, J. Allwood, Feasible supply of steel and cement within a carbon budget is likely to fall short of expected global demand, Nat. Commun. 14 (2023), https://doi.org/10.1038/s41467-023-43684-3.
[2] J. Kim, B.K. Sovacool, M. Bazilian, S. Griffiths, J. Lee, M. Yang, J. Lee, Decarbonizing the iron and steel industry: a systematic review of sociotechnical systems, technological innovations, and policy options, Energy Res. Soc. Sci. 89 (2022), https://doi.org/10.1016/j.erss.2022.102565.
[3] R.M. Andrew, Global CO_2 emissions from cement production, 1928–2018, Earth Syst Sci Data 11 (2019) 1675–1710, https://doi.org/10.5194/essd-11-1675-2019.
[4] B. Shao, Y. Zhu, J. Hu, Y. Zong, Z. Xie, S. Li, W. Du, M. Wang, H. Liu, F. Qian, Chemical engineering solution for carbon neutrality in cement industry: tailor a pathway from inevitable CO2 emission into syngas, Chem. Eng. J. 483 (2024), https://doi.org/10.1016/j.cej.2024.149098.
[5] M. Tomatis, H.K. Jeswani, L. Stamford, A. Azapagic, Assessing the environmental sustainability of an emerging energy technology: solar thermal calcination for cement production, Sci. Total Environ. 742 (2020), https://doi.org/10.1016/j.scitotenv.2020.140510.
[6] World Energy Balances - Data product - IEA, 2024. Https://Www.Iea.Org/Data-and-Statistics/Data-Product/World-Energy-Balances.
[7] G. Lopez, J. Farfan, C. Breyer, Trends in the global steel industry: evolutionary projections and defossilisation pathways through power-to-steel, J. Clean. Prod. 375 (2022), https://doi.org/10.1016/j.jclepro.2022.134182.
[8] Jean-Pierre BIRAT, NET-ZERO STEEL PRODUCTION: WHAT WILL BECOME OF SLAG AND OF ITS VALORISATION? , in: 8th International Slag Valorisation Symposium, Mechelen, Belgium, 2023: pp. 26–29.
[9] F. Bullerjahn, G. Bolte, Composition of the reactivity of engineered slags from bauxite residue and steel slag smelting and use as SCM for Portland cement, Construct. Build Mater. 321 (2022). doi:https://doi.org/10.1016/j.conbuildmat.2022.126331, Constr. Build. Mater..

[10] A.A. Jhatial, I. Nováková, E. Gjerløw, A review on emerging cementitious materials, reactivity evaluation and treatment methods, Buildings 13 (2023), https://doi.org/10.3390/buildings13020526.
[11] P. Vashistha, S. Park, S. Pyo, A review on sustainable fabrication of futuristic cementitious binders based on application of waste concrete powder, steel slags, and coal bottom ash, Int. J. Concr. Struct. Mater. 16 (2022), https://doi.org/10.1186/s40069-022-00541-9.
[12] H.S. Kim, K.S. Kim, S.S. Jung, J.I. Hwang, J.S. Choi, I. Sohn, Valorization of electric arc furnace primary steelmaking slags for cement applications, Waste Manag. 41 (2015) 85–93, https://doi.org/10.1016/j.wasman.2015.03.019.
[13] M. Kirschen, T. Hay, T. Echterhof, Process improvements for direct reduced iron melting in the electric arc furnace with emphasis on slag operation, Processes 9 (2021) 1–10, https://doi.org/10.3390/pr9020402.
[14] J.Y. Lee, J.S. Choi, T.F. Yuan, Y.S. Yoon, D. Mitchell, Comparing properties of concrete containing electric arc furnace slag and granulated blast furnace slag, Materials 12 (2019), https://doi.org/10.3390/ma12091371.
[15] S. Neuhold, A. van Zomeren, J.J. Dijkstra, H.A. van der Sloot, P. Drissen, D. Algermissen, D. Mudersbach, S. Schüler, T. Griessacher, J.G. Raith, R. Pomberger, D. Vollprecht, Investigation of possible leaching control mechanisms for chromium and vanadium in Electric Arc Furnace (EAF) slags using combined experimental and modeling approaches, Minerals 2019, Vol. 9, Page 525 9 (2019) 525. doi:https://doi.org/10.3390/MIN9090525.
[16] M. Kokko, M. Manninen, T. Hu, U. Lassi, T. Vielma, J. Pesonen, Hydrometallurgical recovery of vanadium and calcium from electric arc furnace slag in hydrogen based steelmaking, Miner. Eng. 217 (2024) 108966, https://doi.org/10.1016/J.MINENG.2024.108966.
[17] L. Muhmood, S. Vitta, D. Venkateswaran, Cementitious and pozzolanic behavior of electric arc furnace steel slags, Cem. Concr. Res. 39 (2009) 102–109, https://doi.org/10.1016/j.cemconres.2008.11.002.
[18] A.M. Rashad, A synopsis manual about recycling steel slag as a cementitious material, J. Mater. Res. Technol. 8 (2019) 4940–4955, https://doi.org/10.1016/j.jmrt.2019.06.038.
[19] Y. Zhang, S. Zhang, Y. Chen, O. Çopuroğlu, The effect of slag chemistry on the reactivity of synthetic and commercial slags, Constr. Build. Mater. 335 (2022), https://doi.org/10.1016/j.conbuildmat.2022.127493.
[20] C. Shi, Steel Slag—Its Production, Processing, Characteristics, and Cementitious Properties, J. Mater. Civ. Eng. 16 (2004) 230–236, https://doi.org/10.1061/(asce)0899-1561(2004)16:3(230).
[21] A. Andersson, J. Isaksson, A. Lennartsson, F. Engström, Insights into the Valorization of Electric Arc Furnace Slags as Supplementary Cementitious Materials, Journal of Sustainable Metallurgy 10 (2024) 96–109, https://doi.org/10.1007/s40831-023-00778-y.
[22] A. Barchowsky, M. Aschner, D. Bain, S. Charles, A. Cramb, N. Dejarnett, R. Fry, P. Goodrum, J. Kissel, D. Niemeier, P. O'Day, R. O'Donnell, R. Parkin, D. Walker, R. Wright, R. Wassel, R.S. Duke, K. Guyton, N. Armstrong, A. Depinto, L. Beauchamp, T. Lyles, F.W. Davis, D.B. Barr, A.M. Bartuska, W.A. Chiu, F. Dominici, M. Farooque, R.J. Lewis, M.L. Miranda, M.J. Perry, J. Tewksbury, S. M. Wilson, T.J. Woodruff, L. Llanos, K. Kane, H. Barton, D. Bennett, S. Brantley, T. Cerling, E. Crouch, D. Dorman, H. Gibb, K. Kannan, J. Yzenas, HEALTH RISK CONSIDERATIONS FOR THE USE OF UNENCAPSULATED STEEL SLAG, National Academies Press, 2023, https://doi.org/10.17226/26881.
[23] A.S. Brand, E.O. Fanijo, A review of the influence of steel furnace slag type on the properties of cementitious composites, Appl. Sci. (Switz.) 10 (2020) 1–27, https://doi.org/10.3390/app10228210.
[24] K. Kishore, M.N. Sheikh, M.N.S. Hadi, A critical analysis of electric arc furnace (EAF) slag for sustainable geopolymer concrete production, Mater. Today Sustain. 29 (2025), https://doi.org/10.1016/j.mtsust.2024.101064.
[25] R. Kallio, M. Cantaluppi, J. Louhisalmi, V.V. Visuri, Mineralogical characteristics of fossil-free steel slags, Miner. Eng. 230 (2025), https://doi.org/10.1016/j.mineng.2025.109396.
[26] T. Schade, F. Bullerjahn, G. Bolte, Influence of iron content of chemically and mineralogically modified electric arc furnace slag on the hydration and environmental behaviour of composite cements, Constr. Build. Mater. 441 (2024) 137545, https://doi.org/10.1016/J.CONBUILDMAT.2024.137545.
[27] M. Giels, D.K.A. Michiel, D. Feys, J. Elsen, Y. Pontikes, Transformation of electric arc furnace slag towards reactive supplementary cementitious materials: a pragmatic approach, in: 9th International Slag Valorisation Symposium, 2025, pp. 159–162. Leuven, Belgium.
[28] A. Pfeiffer, G. Wimmer, J. Schenk, Investigations on the Interaction Behavior between Direct Reduced Iron and Various Melts, Materials 15 (2022), https://doi.org/10.3390/ma15165691.
[29] S. Neuhold, D. Algermissen, P. Drissen, B. Adamczyk, P. Presoly, K.P. Sedlazeck, J. Schenk, J.G. Raith, R. Pomberger, D. Vollprecht, Tailoring the FeO/SiO2 ratio in electric arc furnace slags to minimize the leaching of Vanadium and Chromium, Appl. Sci. 2020, Vol. 10, Page 2549 10 (2020) 2549. doi:https://doi.org/10.3390/APP10072549.
[30] C. Zeilstra, J. Small, C. Teerhuis, A. Ehrenberg, M. Bruin, Investigation of slags arising from the HIsarna ironmaking process in building materials application, Proc. 9th International Slag Valorisation Symposium (2025) 192–197. Leuven, Belgium.
[31] R. Kallio, M. Cantaluppi, J. Louhisalmi, V.V. Visuri, Mineralogical characteristics of fossil-free steel slags, Miner. Eng. 198 (2025) 108123.
[32] FEhS-Institut für Baustoff-Forschung, I. Consortium, InSGeP – Investigations of Slags from Next Generation Steel Making Processes, (2023).
[33] K. Schraut, B. Adamczyk, C. Adam, D. Stephan, B. Meng, S. Simon, J. von Werder, Synthesis and characterisation of alites from reduced basic oxygen furnace slags, Cem. Concr. Res. 147 (2021) 106518, https://doi.org/10.1016/J.CEMCONRES.2021.106518.
[34] European Committee for Standardization (CEN), EN 197–1: Cement – Part 1: Composition, specifications and conformity criteria for common cements, 2011.
[35] European Committee for Standardization (CEN), EN 196–1: Methods of testing cement – Part 1: Determination of strength, (2016).
[36] International Organization for Standardization, ISO 5416:2006 — Iron ores — Determination of reducibility by the final degree of reduction index, (2006).
[37] International Organization for Standardization, ISO 9035:1989 — Iron ores — Determination of acid-soluble iron(II) content — Titrimetric method, (1989).
[38] J.S. Ali, H.L. Rutto, T. Seodigeng, S.L. Kiambi, Thermal activation of basic oxygen furnace slag as a heterogeneous catalyst in transesterification: Characterization and catalytic activity studies, Results Eng. 24 (2024) 102899, https://doi.org/10.1016/J.RINENG.2024.102899.
[39] H. Elahidoost, S. Sheibani, S. Raygan, L. Hosseini, A.D. Ahmadabadi, N. Esmaeili, Influence of magnetite concentrate morphology on oxidation and sintering rates of pellet during induration, J. Mater. Res. Technol. 26 (2023) 7116–7126, https://doi.org/10.1016/J.JMRT.2023.09.085.
[40] Bruker AXS GmbH, TOPAS Version 5: General Profile and Structure Analysis Software for Powder Diffraction Data, 2014.
[41] S. Neuhold, D. Algermissen, P. Drissen, B. Adamczyk, P. Presoly, K.P. Sedlazeck, J. Schenk, J.G. Raith, R. Pomberger, D. Vollprecht, Tailoring the FeO/SiO2 ratio in electric arc furnace slags to minimize the leaching of vanadium and chromium, Appl. Sci. (Switz.) 10 (2020). doi:https://doi.org/10.3390/app10072549.
[42] ASTM D5550 - Standard Test Method for Specific Gravity of Soil Solids by Gas Pycnometer, ASTM International 04.08 (2004).
[43] I. Mouedhen, L. Coudert, J.F. Blais, G. Mercier, Prediction of physical separation of metals from soils contaminated with municipal solid waste ashes and metallurgical residues, Waste Manag. 93 (2019) 138–152, https://doi.org/10.1016/j.wasman.2019.05.031.
[44] Y. Grosu, A. Faik, I. Ortega-Fernández, B. D'Aguanno, Natural Magnetite for thermal energy storage: Excellent thermophysical properties, reversible latent heat transition and controlled thermal conductivity, Sol. Energy Mater. Sol. Cells 161 (2017) 170–176, https://doi.org/10.1016/j.solmat.2016.12.006.
[45] X.Y. Cui, S.P. Ringer, G. Wang, Z.H. Stachurski, What should the density of amorphous solids be? J. Chem. Phys. 151 (2019) 194506 https://doi.org/10.1063/1.5113733/198186.
[46] K. Schollbach, M.J. Ahmed, S.R. van der Laan, The mineralogy of air granulated converter slag, Int. J. Ceram. Eng. Sci. 3 (2021) 21–36, https://doi.org/10.1002/ces2.10074.
[47] International Organization for Standardization, ISO 13320:2020 – Particle size analysis — Laser diffraction methods, ISO (2020).
[48] Y. Wang, B. Jiang, Y. Su, X. He, Y. Wang, S. Oh, Hydration and Compressive Strength of Activated Blast-Furnace Slag–Steel Slag with Na2CO3, Materials 2022, Vol. 15, Page 4375 15 (2022) 4375. doi:https://doi.org/10.3390/MA15134375.
[49] S.K. Tripathy, J. Dasu, Y.R. Murthy, G. Kapure, A.R. Pal, L.O. Filippov, Utilisation perspective on water quenched and air-cooled blast furnace slags, J. Clean. Prod. 262 (2020), https://doi.org/10.1016/j.jclepro.2020.121354.
[50] J. Zhao, D. Wang, P. Yan, W. Li, Comparison of grinding characteristics of converter steel slag with and without pretreatment and grinding aids, Appl. Sci. (Switz.) 6 (2016). doi:https://doi.org/10.3390/app6110237.
[51] R. Snellings, J. Chwast, Ö. Cizer, N. De Belie, Y. Dhandapani, P. Durdzinski, J. Elsen, J. Haufe, D. Hooton, C. Patapy, M. Santhanam, K. Scrivener, D. Snoeck, L. Steger, S. Tongbo, A. Vollpracht, F. Winnefeld, B. Lothenbach, RILEM TC-238 SCM recommendation on hydration stoppage by solvent exchange for the study of hydrate assemblages, Materials and Structures/Materiaux et Constructions 51 (2018). doi:https://doi.org/10.1617/s11527-018-1298-5.
[52] Deutsches Institut für Normung, DIN EN 196–11:2019–03 – Methods of testing cement – Part 11: Heat of hydration – Isothermal Conduction Calorimetry method, Deutsches Institut Für Normung (2019).
[53] K. Scrivener, R. Snellings, B. Lothenbach, A practical guide to microstructural analysis of cementitious materials, CRC Press, 2016, https://doi.org/10.1201/b19074.
[54] X., S.R., A.M., A.N.M., B.H.M., B.S., . . . & S.K.L. Li, Reactivity tests for supplementary cementitious materials: RILEM TC 267-TRM phase 1., 2018.
[55] M. Nematzadeh, M. Tayebi, H. Samadvand, Prediction of ultrasonic pulse velocity in steel fiber-reinforced concrete containing nylon granule and natural zeolite after exposure to elevated temperatures, Constr. Build. Mater. 273 (2021) 121958, https://doi.org/10.1016/J.CONBUILDMAT.2020.121958.
[56] M. Tayebi, N. Kamala Ilango, H. Nguyen, A.R. Lori, N. Ranjbar, V. Carvelli, P. Kinnunen, New insights into hydration of MgO in the presence of polycarboxylate ether superplasticizers, Cem. Concr. Compos. 162 (2025) 106153, https://doi.org/10.1016/J.CEMCONCOMP.2025.106153.
[57] UltraTest GmbH. UltraTestLab V7 [computer software]. Achim, Germany. Available from: https://ultratest.de/ip-8-messurement-system, (n.d.).
[58] B.H.U. Tekle, L. Hertwig, K. Holschemacher, Setting Time and Strength Monitoring of Alkali-Activated Cement Mixtures by Ultrasonic Testing, Materials 2021, Vol. 14, Page 1889 14 (2021) 1889. doi:https://doi.org/10.3390/MA14081889.
[59] A. Naqi, B. Delsaute, M. Königsberger, S. Staquet, Effect of solution-to-binder ratio and alkalinity on setting and early-age properties of alkali-activated slag-fly ash binders, Materials 2023, Vol. 16, Page 373 16 (2022) 373. doi:https://doi.org/10.3390/MA16010373.
[60] Brussels: European Committee for Standardization, in: EN 450–1:2012 – Fly ash for concrete – Part 1: Definition, specifications and conformity criteria, 2012.
[61] PANalytical B.V. HighScore Plus. Almelo, The Netherlands: PANalytical., (n.d.).

[62] European Committee for Standardization (CEN), Characterisation of Waste — Leaching — Compliance Test for Leaching of Granular Waste Materials and Sludges — Part 2 (EN 12457–2), 2002.
[63] Environment – Analyses of selected elements in water, eluates and destruates, Atomic emission spectrometry with inductively coupled plasma (NEN 6966), Nederlands Normalisatie-Instituut (NEN), 2005.
[64] Soil Quality Decree (Besluit bodemkwaliteit), Government of the Netherlands, 2007.
[65] A. Schöler, F. Winnefeld, M. Ben Haha, B. Lothenbach, The effect of glass composition on the reactivity of synthetic glasses, J. Am. Ceram. Soc. 100 (2017) 2553–2567. doi:https://doi.org/10.1111/JACE.14759;PAGE:STRING:ARTICLE/CHAPTER.
[66] X. Li, M. Cao, Recent Developments on the Effects of Micro- and Nano-Limestone on the Hydration Process, Products, and Kinetics of Cement, Materials 2024, Vol. 17, Page 2133 17 (2024) 2133. doi:https://doi.org/10.3390/MA17092133.
[67] D.P. Bentz, T. Sato, I. De La Varga, W.J. Weiss, Fine limestone additions to regulate setting in high volume fly ash mixtures, Cem. Concr. Compos. 34 (2012) 11–17, https://doi.org/10.1016/J.CEMCONCOMP.2011.09.004.
[68] S. Adu-Amankwah, M. Zajac, C. Stabler, B. Lothenbach, L. Black, Influence of limestone on the hydration of ternary slag cements, Cem. Concr. Res. 100 (2017) 96–109, https://doi.org/10.1016/J.CEMCONRES.2017.05.013.
[69] H. Ye, A. Radlińska, A Review and Comparative Study of Existing Shrinkage Prediction Models for Portland and Non-Portland Cementitious Materials, Adv. Mater. Sci. Eng. 2016 (2016) 2418219, https://doi.org/10.1155/2016/2418219.
[70] B. Lothenbach, K. Scrivener, R.D. Hooton, Supplementary cementitious materials, Cem. Concr. Res. 41 (2011) 1244–1256, https://doi.org/10.1016/J.CEMCONRES.2010.12.001.
[71] S. Solismaa, A. Torppa, J. Kuva, P. Heikkilä, S. Hyvönen, P. Juntunen, M. Benzaazoua, T. Kauppila, Substitution of Cement with Granulated Blast Furnace Slag in Cemented Paste Backfill: Evaluation of Technical and Chemical Properties, Minerals 2021, Vol. 11, Page 1068 11 (2021) 1068. doi:https://doi.org/10.3390/MIN11101068.
[72] B.V. Kiwa Nederland, Assessment guideline BRL 1804: Filler for use in concrete and mortar, 2019.
[73] R. Snellings, G. Mertens, Ö. Cizer, J. Elsen, Early age hydration and pozzolanic reaction in natural zeolite blended cements: Reaction kinetics and products by in situ synchrotron X-ray powder diffraction, Cem. Concr. Res. 40 (2010) 1704–1713, https://doi.org/10.1016/J.CEMCONRES.2010.08.012.
[74] Wei Chen, Hydration of slag cement-Theory, University of Twente, Modelling and Application, 2007.
[75] E. Horszczaruk, Properties of cement-based composites modified with magnetite nanoparticles: a review, Materials 2019, Vol. 12, Page 326 12 (2019) 326. doi:https://doi.org/10.3390/MA12020326.
[76] N.K. Katyal, S.C. Ahluwalia, R. Parkash, Effect of barium on the formation of tricalcium silicate, Cem. Concr. Res. 29 (1999) 1857–1862, https://doi.org/10.1016/S0008-8846(99)00172-6.
[77] I.G. Richardson, Clarification of possible ordered distributions of trivalent cations in layered double hydroxides and an explanation for the observed variation in the lower solid-solution limit, Urn:Issn:2052–5192, Acta Crystallogr. Sect. B Struct. Sci. Cryst. Eng. Mater. 69 (2013) 629–633, https://doi.org/10.1107/S2052519213027905.